Large Eddy Simulations of the Dusty Martian Convective Boundary Layer with MarsWRF

Zhaopeng Wu[1,2]*, Mark I. Richardson[3], Xi Zhang[4], Jun Cui[1,2,5], Nicholas G. Heavens[6,7], Christopher Lee[3,8], Tao Li[2,9], Yuan Lian[3], Claire E. Newman[3], Alejandro Soto[10], Orkun Temel[11,12], Anthony D. Toigo[13], and Marcin Witek[14].

[1] School of Atmospheric Sciences, Sun Yat-Sen University, Zhuhai, Guangdong, People's Republic of China

[2] CAS Center for Excellence in Comparative Planetology, Hefei, Anhui, People's Republic of China

[3] Aeolis Research, Chandler, AZ, United States

[4] Department of Earth and Planetary Sciences, University of California Santa Cruz, Santa Cruz, California, United States

[5] CAS Key Laboratory of Lunar and Deep Space Exploration, National Astronomical Observatories, Chinese Academy of Sciences, Beijing, People's Republic of China

[6] Space Science Institute, 4765 Walnut St, Suite B, Boulder, CO 80301

[7] Department of Atmospheric and Planetary Sciences, Hampton University, Hampton, VA, 23668, United States

[8] Department of Physics, University of Toronto, St. George, Toronto, Ontario, M5S 1A7, Canada

[9] CAS Key Laboratory of Geospace Environment, School of Earth and Space Sciences, University of Science and Technology of China, Hefei, Anhui, People's Republic of China

[10] Southwest Research Institute, Boulder, CO, USA

[11] FU Leuven, Institute of Astronomy, Leuven, Belgium

[12] Royal Observatory of Belgium, Brussels, Belgium

[13] Johns Hopkins University Applied Physics Laboratory, Laurel, MD 20723, United States

[14] Jet Propulsion Laboratory, Pasadena CA, United States

Key points:

1. Dust radiative-dynamical feedbacks upon turbulent mixing in the Martian boundary layer is studied by Large eddy simulation with MarsWRF.
2. The destabilizing effect of dust lateral heating contrasts is found to augment convection greatly deepening the boundary layer.
3. Under some circumstances a positive feedback may exist among dust radiative heating, the intensity of boundary layer mixing, and dust lifting.

Abstract

Large eddy simulation (LES) of the Martian convective boundary layer (CBL) with a Mars-adapted version of the Weather Research and Forecasting model (MarsWRF) is used to examine aerosol dust radiative-dynamical feedback upon turbulent mixing. The LES is validated against spacecraft observations and prior modeling. To study dust redistribution by coherent dynamical structures within the CBL, two radiatively-active dust distribution scenarios are used—one in which the dust distribution remains fixed and another in which dust is freely transported by CBL motions. In the fixed dust scenario, increasing atmospheric dust loading shades the surface from sunlight and weakens convection. However, a competing effect emerges in the free dust scenario, resulting from the lateral concentration of dust in updrafts. The resulting enhancement of dust radiative heating in upwelling plumes both generates horizontal thermal contrasts in the CBL and also increases buoyancy production, jointly enhancing CBL convection. We define a dust inhomogeneity index (DII) to quantify how much dust is concentrated in upwelling plumes. If the DII is large enough, the destabilizing effect of lateral heating contrasts can exceed the stabilizing effect of surface shading such that the CBL depth increases with increasing dust optical depth. Thus, under certain combinations of total dust optical depth and the lateral inhomogeneity of dust, a positive feedback may exist among dust optical depth, the vigor and depth of CBL mixing, and—to the extent that dust lifting is controlled by the depth and vigor of CBL mixing—the further lifting of dust from the surface.

Plain Language Summary

We use a very high-resolution atmospheric model (MarsWRF) to study the interaction between dust and turbulent motions at the bottom of the Martian atmosphere. The model is validated against satellite observations and previously validated model results. Two types of experiment are conducted to test the effect of the horizontal dust distribution. With horizontally uniform dust levels, increasing the total dust amount cools the surface

and weakens convective motions called updrafts, just as pan of water becomes less turbulent as the stove is turned down. However, if the dust is allowed to move horizontally in the domain, updrafts tend to concentrate the dust and become dustier than average. Dust contained in the updrafts is then heated by the Sun and become stronger. If atmospheric dust is distributed very unevenly, the effect of stronger temperature differences may exceed the updraft-weakening effect of dust cooling the surface, resulting in taller updrafts as atmospheric dust increases. Because stronger updrafts and convection may lead to greater dust lifting, this study shows how weather systems on Mars can be strengthened and maintained by mobilizing dust from the surface.

1. Introduction

Suspended mineral aerosol dust provides a significant contribution to the meteorological and climatological forcing on Mars, due to the widespread availability of dust on the surface, the frequent occurrence of dust lifting events (due to surface wind stress, dust devils, or other processes), the relative inefficiency of scavenging processes when little water is present, and the strong interaction of dust with both visible and thermal infrared radiation in the thin Martian atmosphere [*e.g., Kahre et al., 2017; Martinez et al*., 2017]. The dust thermal forcing and the dynamics of the atmosphere are coupled through the fact that atmospheric motions both change the distribution of dust in the atmosphere and the rate of dust injection from the surface, and that the distribution and amount of dust modifies atmospheric motions through its influence on radiative heating. Some of the atmospheric transport of dust and all of the lifting of dust from the surface occurs within the planetary boundary layer (PBL, also known as the convective boundary layer, CBL, in the daytime). The PBL is the atmospheric layer, typically within 10 km of the surface, where thermally and mechanically forced turbulence (natural and forced convection, respectively) dominates atmospheric dynamics [*Goody and Belton*, 1967; *Petrosyan et al*., 2011]. Strong vertical motions within CBL can occur on multiple horizontal scales, ranging from many

kilometers down to meters. The largest lateral scales of several tens of kilometers correspond to quasi-cellular thermal convection for the deepest PBL depths and cell aspect ratios of 1-4 [*e.g., Zhou et al*., 2014]. These cellular structures approximate idealized Rayleigh–Bénard convection cells (or simply Bénard cells), especially in the lower CBL, and are the eponymous "large eddies" that are fully resolved with LES. Strong vertical motions at meter scales correspond to the updrafts in the cores of small convective vortices, which, if dusty, are called dust devils [*e.g. Toigo et al.*, 2003; *Michaels and Rafkin*, 2004; *Colaïtis et al.*, 2013]. Some fraction of the convective vortex size spectrum may be captured by LES—but generally not all, depending on the specific LES resolution chosen.

While the Martian PBL and CBL has been examined in some detailed with LES and to a more limited degree with observations [e.g., *Petrosyan et al*., 2011; *Spiga*, 2019], the LES studies thus far have used laterally uniform dust heating. However, dust in the lower martian atmosphere often exhibits lateral structure, from distinct dust devil plumes to implied convective granularity in dust clouds [*e.g., Fisher et al.*, 2005; *Inada et al.*, 2007; *Määtänen et al* .2009; *Guzewich et al*., 2015]. These observations and the known radiative properties of dust motivate the question of whether the spatial distribution of dust can feed back onto the dynamics of dust transport through the radiative effects of dust modifying the CBL and hence also the injection of dust from the surface into the atmosphere [*e.g*., *Fuerstenau*, 2006; *Heavens et al*., 2011; *Daerden et al.*, 2015]. Of specific importance are the questions of whether the radiative heating due to the lateral concentration of dust modifies: 1) the altitudes to which dust can be transported; 2) the vigor and depth of the PBL circulation; and, 3) the distribution of surface wind stresses that drive dust lifting from the surface. Current parameterizations of PBL physics used in global and mesoscale models do not include the effects of lateral dust variations—and consequent radiative feedback—within CBL circulation structures and thus may incorrectly represent the response of the PBL, and dust vertical mixing and lifting, to a given vertical atmospheric temperature and

wind profile, or to atmospheric dust loading. The purpose of this study is to investigate the degree and nature of the feedback between dust lateral inhomogeneity and PBL convective motions. Since we focus exclusively on thermally forced PBL motions (*i.e.*, free convection), we henceforth use the more specific designation CBL.

In this study, we use the Mars Weather Research and Forecasting (MarsWRF) model [*Richardson et al.*, 2007; *Toigo et al.*, 2012; *Lee et al.*, 2018] in its large eddy simulation (LES) configuration in order to directly resolve much of the spectrum of motions in the CBL. LES is designed to capture the largest scales of motion within the CBL (*i.e.*, motions on the microscale), but is not designed to represent motions on larger scales such as mesoscale or synoptic/global scales, which are either ignored or imposed as uniform boundary conditions. Since real atmospheric motions occur over a continuum size spectrum scale, it is not possible to perfectly categorize motions into distinct scales. However, the two dividing lines between the micro-, meso-, and synoptic scales represent real "clustering" of motions on scales determined on the lower end by the maximum size of PBL convection (in this paper, we take this to be roughly 10 km) and at the larger end, by the minimum scale of baroclinic eddies (which is unimportant for this paper, but which we take to be roughly 500 km). LES is also not designed to represent motions on the smallest scales of motion (*i.e.*, Kolmogorov scales) that are important for thermal and mechanical dissipation. This distinguishes LES from Direct Numerical Simulation (DNS) and means that LES still requires parameterization of eddy diffusion. In practice, the grid spacing of LES is typically set at 1-100 m, and this is done in order to make LES of meaningful PBL dynamics computationally tractable.

In this paper, the MarsWRF LES model is described in Section 2, where we discuss the model configuration, physics parameterizations including the treatment of aerosols, and the two specific dust distribution scenarios used in this study. In Section 3, we describe

LES cases with a fixed dust scenario matching the times and locations of radio science observations described by *Hinson et al.* [2008] (specifically their cases *a*, *b*, *c* and *i*). These observations have also been simulated with the related LMD-LES model [*Spiga et al.*, 2010] and we use the comparison to validate the performance of MarsWRF-LES. In Section 4, we set up several experiments to explore the effects of our two dust distribution scenarios—the fixed dust scenario and the variable scenario—on the CBL evolution. In Section 5, we examine the effect of dust concentration in the CBL on the distributions of radiative heating and on the vertical and horizontal winds. We specifically quantify the response of the CBL in terms of a Dust Inhomogeneity Index (DII). Finally, in Section 6, we summarize the major findings of this work and provide some discussion.

2. Model Description

We simulate the Martian CBL using the MarsWRF model [*Richardson et al.*, 2007], a Mars-adapted version of National Center for Atmospheric Research (NCAR) WRF model that has been used for terrestrial LES extensively over the last decade [*Powers et al.*, 2017]. *Richardson et al.* [2007] showed a limited set of LES using MarsWRF, but the model setup and the model performance were not described in detail. WRF also functions as the dynamical core for the Laboratoire de Météorologie Dynamique (LMD) Mars LES but using independently develeoped physics [*Colaïtis et al.*, 2013; *Spiga et al.*, 2017].

The MarsWRF model used in this study is based on the WRF release version 3.3.1 (see the NCAR WRF website http://wrf-model.org for more information on model versioning). The model is essentially identical to that used most recently for simulating winds and surface pressure at the Curiosity landing site [*Newman et al.*, 2017; *Richardson and Newman*, 2018] and synoptic-scale solstitial pause of high-latitude transient eddy activities [*Lee et al.*, 2018]. The MarsWRF model is capable of simulating atmospheric dynamics with a wide range of length scales across the micro-, meso- and synoptic scales. The structured "C-grid"

WRF mesh can be configured to cover the whole planet as a traditional General Circulation Model (GCM) or as limited area mesoscale or microscale (LES) domains. In this study, the LES mesh is treated as an idealized domain with doubly periodic boundary conditions. This can be thought of as creating an effectively boundaryless infinite plane, though motions on scales larger than half the mesh extent are suppressed by the periodicity.

The model includes a two-stream radiative transfer code that simultaneously provides atmospheric and surface heating rates due to gases and aerosols in both visible and thermal infrared wavelengths [*Mischna et al.*, 2012]. The surface temperature and the sensible heat flux may be either prescribed or prognostically-evolved by the model. The prognostic scheme treats the surface energy balance and the diffusion of heat within a multi-layer subsurface model. Topography, surface albedo, thermal emissivity, and subsurface thermal diffusivity may be set as constants or using maps generated from orbiter data sets. While in this paper we use laterally uniform surface and subsurface properties, the LES-configured model is currently able to ingest high resolution digital terrain elevation products.

While LES is designed to capture the largest scales of CBL motions, it does not resolve all motions down to the scales of dissipation (*i.e.*, it is not direct numerical simulation, DNS, which is too computationally expensive for practical use in CBL modeling). Instead, a Sub-Grid Scale (SGS) (often also referred to as Sub-Filter Scale, SFS) parameterization is used, which in the simulations described in this paper is implemented as a diffusion of heat, momentum, and tracers. The scheme calculates the diffusivity and viscosity based on a prognostic value of turbulence kinetic energy (TKE) evolved using resolved variables. The SGS/SFS TKE scheme is discussed in more detail in Appendix A, as is its relationship to the other widely used SGS/SFS in WRF, the three-dimensional Smagorinsky scheme.

2.1 Fixed and Variable Atmospheric Dust

The atmospheric radiative transfer code requires information on the spatial distribution, the composition, and the size distribution of aerosols in the atmosphere. This information can be either prescribed or prognostically-evolved in the model. In this work, we use a prescribed "fixed dust scenario" to provide control cases, and a prognostic simulation in order to examine the importance of spatial variation of dust, the "variable dust scenario". In both cases, the optical properties of dust remain fixed in the simulations. They are calculated using Mie scattering and assuming a fixed dust size distribution employing a modified gamma size distribution with effective radius, r_{eff}=1.7μm, and effective variance, ν_{eff} =0.4, and using indices of refraction from Wolff and Clancy [2003]. The reference wavelength used for optical depth is 0.67μm and thus in this paper we refer to visible optical depths.

In the "fixed dust" (FD) cases, dust is prescribed to vary in the vertical according to a modified Conrath distribution [*Conrath*, 1975; *Montmessin et al*., 2004] which corresponds to constant dust mass mixing ratio up to a capping altitude, and with the dust uniformly distributed in the horizontal and not varying with time. Since in this study, the LES model top is generally placed at 12-15 km, the Conrath profile yields an almost uniform vertical dust mass mixing ratio profile. While the dynamical model top is placed at 12-15 km, the radiative transfer scheme treats absorption, scattering, and (for the infrared) emission through the full column depth. However, dust opacity is only present within the depth covered by the dynamical model, and thus the optical depths reported here correspond to the cumulative optical depths between the surface and the dynamical model top at 12-15km.

The "variable dust" (VD) cases allows the dust distribution to evolve spatio-temporally by parameterizing dust lifting, transport, and sedimentation. For this scenario, a single dust tracer bin is used to perform sedimentation, transport by resolved winds, and diffusion by

subgrid scale turbulence [*Newman and Richardson*, 2015]. A representative size of 2μm radius is chosen for the dust particles for the purposes of sedimentation (the size is unimportant for the other physical and dynamical processes). The simulations are initialized with a modified Conrath profile of dust, which except where stated, corresponds to a column optical depth of 0.3. In these simulations, microphysical interactions with water are not used (the LES cases described here are dry, *i.e.*, there is no water ice or water vapor in the model). At the surface, resolved winds are used to lift dust via the wind stress lifting parameterization described in *Newman and Richardson* [2015], in which dust is injected into the lowest model layer whenever the wind stress exceeds a constant threshold. The rate of dust injection, Q_s, is determined following *Newman and Richardson* [2015] as:

$$Q_s = max\left[0, \left(\alpha_N \frac{\rho}{g} u_{drag}^3 \left(1 - \frac{u_{drag}^t}{u_{drag}}\right)\left(1 + \frac{u_{drag}^t}{u_{drag}}\right)^2\right)\right] \quad (1)$$

Where ρ is the near-surface air density, g is acceleration due to gravity, u_{drag} is the frictional velocity, and u^t_{drag} is the threshold fractional velocity; and where $u_{drag} = (\tau/\rho)^{1/2}$, with τ being the atmospheric shear stress at the surface. For our experiments, we chose the value of τ^t, the threshold wind stress, and use it in the frictional velocity equation to determine the u_{drag}^t value then used in Eqn. 1. The lifting rate parameter, α_N, is a free parameter that we chose and then hold constant for a given simulation. For simplicity, we do not include any parameterization for lifting of dust associated with the rapid change of surface pressure within convective vortices [*e.g.*, *Neakrase et al*, 2006]. As with the FD cases, there is no dust optical depth above the dynamical model top in the VD cases.

3. Model Consistency and Observational Validation

High vertical resolution measurements covering the entire vertical extent of the CBL are rare on Mars, which limits efforts to directly validate LES. *In situ* near surface and tower

observations, which are crucial for LES validation on Earth, are very limited or non-existent, respectively, on Mars. Of the remotely sounded observations from orbit, radio occultation measurements of thermal structure provide one of the best constraints due to the relatively high vertical resolution (roughly 100m), albeit with extremely long lateral sampling lengths through the limb (roughly 400km) [*e.g.*, *Hinson et al.* 2008]. Hinson *et al*. [2008] use Mars Express radio occultation measurements, isolating profiles that provided good coverage of the well-developed CBL in tropical latitudes and located sufficiently far from large topographic relief that the profiles could be taken as representative of a relatively uniform CBL over the long lateral observational path. Based on these observations, *Hinson et al.* [2008] investigated the depth of the CBL in the low-latitude regions. Specifically, the observations highlighted a dependence of the CBL depth on the background thermal structure, the surface temperature, and the surface air density that is extremely useful for our purposes as the dependence can be used to quantitatively validate (or invalidate) the performance of the LES. Indeed, *Spiga et al.* [2010] conducted an extensive analysis of these radio occultation profiles with the LMD-LES model—which also uses the WRF dynamical core but is forced with a completely different set of physics—and thus the combination of the *Hinson et al.* [2008] observations and the *Spiga et al.* [2010] profile simulations and derived model quantities provide a very convient means of testing both the degree to which MarsWRF LES can reproduce observations and the degree to which MarsWRF LES is consistent with other published LES performance.

In this section, we describe simulations undertaken with fixed dust scenarios and with the physical parameterizations as described in Section 2, including the prognostic treatment of ground temperature and surface layer mixing. We specifically describe simulations designed to replicate the times and locations labeled cases *a*, *b*, *c* and *i* by *Hinson et al.* [2008] and as also used by *Spiga et al.* [2010]. For ease of comparison with those prior

works, the location and forcing information for the four cases are given in Table 1 along with a limited sample of prognostic summary information from our LES.

The default LES numerical mesh use 145×145×100 grid points (the two horizonal directions and finally the vertical direction) with 100 m horizontal resolution and a 15 km model top, similar to that used by *Spiga et al.* [2010]. The mesh lateral and vertical extents were chosen to accomodate the largest expected convective cell sizes based on the radio science estimates of the CBL depth [*Hinson et al.,* 2008] and expected aspect ratios of 1-4 for Rayleigh-Bénard-like convection. In the vertical, we adopted an increasingly stretched grid with each layer 3.5% thicker than the one below it so that the grid depth near the surface is on the order of 10m to ensure high enough vertical resolution for the simulation of the shallow surface layer. The timestep *dt* is 1s. Table 1 shows the solar longitude (Ls), latitude, longitude, thermal inertia, albedo, and surface roughness the four cases, and these were chosen to be the same as those used by *Spiga et al.* [2010]. The LES was set up with doubly periodic lateral boundary conditions, no externally imposed wind was applied (*i.e.*, the background wind was zero), and the dust was set up such that the visible (0.67 micron) dust optical depth was 0.3. The model was initialized using the Mars Express radio occultation pressure-temperature profiles as retrieved by *Hinson et al.* [2008]. Each run was initialized at 5 PM local time (henceforth we will use 24 hour clock designation and the LT acronym for local time, *e.g.*, 5 PM is 1700 LT, note also that both the MarsWRF LES and LMD-LES models used true local solar time, which was also employed for the radio science observations). In order to seed the model with some initial turbulence, slight random perturbations were added to the temperature (with a maximum amplitude of 0.2% of the full temperature). Each simulation was then allowed to run overnight to allow the LES to ‘spin up’ and we examined output from the following simulated Sol.

To determine the CBL height from the model thermal profile, we follow the method used in *Hinson et al.* [2008] and *Spiga et al.* [2010]. The static stability, S, is defined as:

$$S(z) = \frac{\partial T}{\partial z} + \frac{g}{c_p} \quad (2)$$

Where T is the air temperature, z is the vertical height, g is the acceleration due to gravity and c_p is the specific heat capacity of air at constant pressure. Using Eqn. 2, S is calculated from the mean atmospheric temperature profiles. The CBL height z_i is defined as the altitude above the surface where S first reaches 1.5 K/km. The evolution of the CBL height with local time during the four cases is shown in Figure 1a. All four cases exhibit typical CBL daytime growth. The CBL height grows very slowly before 0900LT as the overlaying nocturnal stable layer is progressively eroded and overcome. After that, the CBL begins to entrain the residual layer and grows rapidly until about 1500LT, after which time it maintains a reasonably constant maximum depth until the observation (or "forecast") time at 1700LT.

The CBL top heights (or "CBL depths," the two terms mean the same thing in this context) of cases a, b, c and i predicted by MarsWRF at 1700LT are about 6.1km, 5.7km, 7.9km and 7.3km, respectively (Table 2). These compare with Hinson *et al.* [2008] observational estimates of 5.1km, 4.2km, 8.2km, and 10km, respectively, for the real atmospheric profiles. We can see dramatic variations of CBL height in different locations (cases c and i much higher than cases a and b) which was even more dramatically indicated in *Hinson et al.* [2008]. This site-to-site variability is caused the very different elevations of the two groups of sites, with a and b at much lower elevation than c and i [*Hinson et al*., 2008]. The elevation has two primary effects: 1) A site at higher elevation means a lower surface pressure (the surface pressure in our case c is only about 55% of that in our case a), and hence a similar amounts of sensible heat flux into a much thinner atmosphere would lead

to a much larger heating rate, and hence a deeper CBL than a low elevation site; 2) The atmosphere a few kilometers above the surface into which the CBL is expanding will generally be cooler at the higher geopotential over a high elevation surface than it will at the same relative altitude over a low elevation surface (see Figure 5A from *Hinson et al*. [2008]). As a result of these effects, the convective available potential energy of CBL thermals is larger over higher elevation surfaces which means convection can reach a higher altitude and produce a deeper CBL at these sites.

Despite similar trends, LES predicts a more limited range of CBL depths than is inferred from the observations (Table 2). The observations suggest an almost 6 km difference in depth between the minimum and maximum cases (b and i, respectively), with the i case observationally inferred to be almost 2.4 times deeper than the b case, while MarsWRF suggests it is only 1.8km or 30% deeper. However, this under-prediction of the influence of surface elevation on the CBL depth is also present in the LMD-LES results presented by *Spiga et al.* [2010] and included for reference in Table 2. *Spiga et al.* [2010] find the case a, b, c, and i CBL to be 5.9km, 5.3km, 7.8km and 7.4km, respectively. MarsWRF thus is in much better agreement with the LMD-LES (showing only a 100-400m discrepancy between the models) than either LES is with the observational inference (discrepancies of 300m-2.7km); though it should be noted that both models show the same sign of the behavior as the observations (*i.e*., lower elevation surfaces have shallower CBL depths).

The similar model behavior regarding CBL depth is also reflected directly in the thermal predictions: the maximum surface temperatures of the four MarsWRF cases shown in Table 1 are close to those predicted by *Spiga et al.* [2010] (within 4 – 9 K), and the mixed layer potential temperatures at 1700LT are similar to those in *Spiga et al.* [2010] except for case c. Modest discrepancies between the models may result from several factors. First, while a dust optical depth, τ=0.3, was used both here and by Spiga *et al.* [2010], the

radiative transfer schemes, the dust optical properties, and the specific details of the vertical distribution of dust were slightly different between the LMD-LES and MarsWRF. The daytime maximum ground temperature is especially sensitive to the amount of sunlight reflected by the atmospheric dust. Second, we have used the Mars Express radio occultation profiles for the initial model thermal structure while *Spiga et al.* [2010] used output from a GCM, and our simulations are started in the late afternoon, and thus have a longer spin-up period that covers the whole night. While the evening collapse of the CBL and the subsequent reestablishment after dawn mean that the MarsWRF case is likely less dependent upon the initialization, this may or may not be an advantage depending on a number of factors, including the degree to which the model mean state drifts away from the observed state.

Despite very minor differences, our results reveal essentially the same qualitative and quantitative behavior when the two models simulate the four cases. The CBL depth trends shown in Figure 1a for the MarsWRF LES compare well with those from the LMD-LES shown in Figure 2 from *Spiga et al.* [2010]. Picking one case as an illustrative example, the increase of the CBL height in case i is slower than the other cases in the morning, but faster at noon and in the early afternoon. This is consistent with the evolution of surface temperatures shown in Figure 1b, which supports the *Spiga et al.* [2010] suggestion that the slower growth of the CBL for case i before 1400LT is due to the larger surface thermal inertia at this site. We also compared the MarsWRF and LMD-LES turbulent kinetic energy, vertical eddy heat flux, and the updraft maximum vertical velocities for cases where plots were available in *Spiga et al.* [2010], with the models agreeing well (detailed comparison is not shown here for brevity). From a purely modeling perspective, we conclude that MarsWRF and the LMD-LES produce very similar simulations of the CBL under similar conditions. This similarity in performance likely results from 1) the use of a nearly identical dynamical core, and 2) the use of a physics suite that while wholly different

at a codebase level has, akin with the LMD Mars physics, been developed to well simulate available observations of Mars.

The quantitative differences between the CBL depths produced by either LES model and the observations suggests a consistent error in one or more of: 1) the estimated surface properties (albedo, thermal inertia, *etc*.), 2) the specification of aerosol atmospheric radiative heating (or other radiative heating rate errors), 3) the representation of the surface layer fluxes into the lowest model layer, or 4) the fidelity of the WRF dynamical core and/or SGS/SFS parameterization in simulating large PBL eddies in the Martian atmosphere. The second and third sources of error would require correlated errors between the separate MarsWRF and LMD physics, which may seem less likely, but might result from the "herd effect" that can influence physics package development as groups tend not to want to be the "outlier" group in intercomparison efforts. The fourth source of error seems the least likely of the four due to the extensive testing of the dynamical core by the terrestrial community (but we cannot rule out a consistent misapplication of the core to Mars in terms of choice of grid setup, etc.) Notwithstanding these concerns, we agree with the *Spiga et al.* [2010] conclusion that, given the uncertainty in the observations of both the atmospheric state and forcing, LES does an acceptably good job quantitatively representing the CBL, and a much better job qualitatively, and that we can thus reasonably use the MarsWRF LES as a calibrated tool with which to gain quantitative insight into the behavior of the CBL.

3.1 Sensitivity of LES to Mesh Extent and Spacing

To evaluate the effect of different model grid setups on the LES, we used the Hinson/Spiga case i to carry out a sensitivity study for MarsWRF using seven numerical mesh definitions shown in Table 3. Using z_i, the predicted thickness of the 1700LT CBL as the primary diagnostic (see the last column of the table), Table 3 allows us to draw several conclusions

regarding the sensitivities of the model to the mesh setup. Firstly, the results are insensitive to the horizontal resolution within a range between 10m to 100 m (see meshes 1 and 2) and to the model top height as long as the model top is sufficiently higher than the CBL depth (see meshes 2 and 3). Secondly, while meshes 2 and 4 share similar horizontal resolution, the CBL depth of mesh 4 is ~300 m lower than mesh 2, which results from the horizontal domain extent being smaller than the maximum CBL height. Since the width-to-depth aspect ratio of the largest CBL eddies (which are hence the CBL maximum scale setting eddies) is expected to be about 1-4, this tells us the horizontal domain extent should be more than four times larger than (or at the very minimum, comparable to) the maximum CBL height in order to ensure that the CBL is not being numerically compressed (see meshes for which $x \geq z_i$). Note that while this might paradoxically seem to suggest that the maximum CBL height needs to be known before the domain extent can be chosen, the minimum domain extent can in fact be found by increasing the domain extent until the maximum CBL depth no longer increases with increasing domain extent. Thirdly, too coarse vertical resolution will lower the CBL height (compare meshes 4 and 6). The above findings are in agreement with the sensitivity study of different extent and resolution of the LES grid by *Spiga et al*. [2010]. As a result, we use numerical mesh 3 as the default configuration for the rest of this work to obtain accurate results with the lowest computational cost. For our implementation of the Hinson/Spiga case i using numerical mesh 3, the dynamical model top pressure, p_{top}=142.889 Pa.

4. CBL Development as a Function of Optical Depth in Fixed and Variable Dust LES

The primary question motivating this paper is whether lateral heterogeneity of dust within the CBL during active dust lifting causes any changes in the strength and/or depth of the CBL from that which would occur if the dust were uniform. Such differences in behavior might provide a better guide into how deep into the atmosphere dust is lofted from the surface, and into potential radiative-dynamical feedback processes involving dust lifting

and the CBL. In order to address this question, in this section we devise two sets of LES experiments, one in which dust is uniformly distributed, and one in which the dust is injected at the surface and the dust distributions are allowed to freely evolve based on model resolved winds and SGS/SFS diffusion (see Section 2). In the fixed dust cases, the total dust optical depth is the only free parameter, with all remaining parameters being set following the Hinson/Spiga case *i* settings described in Section 3 (Tables 1 and 2) and using numerical mesh 3 (Table 3). In the variable dust cases, only the injection rate constant used in the stress lifting scheme is used as a free parameter (see Section 4.2), again with all other parameters being held fixed at values from Hinson/Spiga case *i* and numerical mesh 3. The injection rate parameter is also held constant with time in each variable dust simulation. For comparison between fixed and variable dust cases, we select the variable dust LES case from an ensemble that has the desired total column optical depth at a given local time in order to compare with a given fixed dust case.

4.1 Fixed Dust Cases

For fixed dust LES, we vary only the prescribed and non-time varying abundance of atmospheric dust, which modifies the total column dust optical depth at all wavelengths. The six-member "fixed dust" ensemble comprises cases yielding visible optical depth values of 0 (*i.e.*, clear or "dust free"), 0.1, 0.2, 0.3, 0.4 and 0.5. We label these cases FD0, FD1, FD2, FD3, FD4, and FD5, respectively. In Figure 2, we show the diurnal variation of the domain average values of the CBL height (Fig. 2a), the surface temperature (Fig. 2d), the CBL or mixed layer average potential temperature (Fig. 2g), and the difference between the ground temperature and the kinematic air temperature at 10m altitude (Fig. 2j).

Fig. 2a and 2c show that the net effect of increasing the dust loading is to significantly decrease the depth of the mature CBL. At 1700 LT, the clear atmosphere CBL is just over 9.5km deep, with each increment of 0.1 of optical depth, the 1700 LT CBL depth decreases

to 9.0km, 7.8km, 7.3km, 6.3km, and 5.7km, respectively. Thus, the CBL depth decreases by about 40% when the visible optical depth is increased from 0 to 0.5 (Fig. 2c).

As shown in Fig. 2d and 2g, the surface temperature decreases while the mixed layer potential temperature increases with dust optical depth (Fig. 2f and 2i). Thus, the decrease in the mature CBL depth results from the rather straightforward combined effect of: 1) increased atmospheric dust radiative heating of the atmosphere due to the increased atmospheric absorption of sunlight, and 2) cooling of the surface due to the increased shading of the ground from solar insolation by atmospheric dust scattering and absorption. These related effects act to increase the static stability of the atmosphere and decrease the sensible heat flux from the ground as optical depth increases (Fig. 2l), and hence decrease the buoyant production of turbulence.

Fig. 3a shows that the peak vigor of CBL mixing (at about 1330-1400 LT) is also decreased as a result of increased optical depth (*i.e.*, the increased optical depth does more than simply decrease the depth of the CBL). Fig. 3a shows a decrease in the average strength of updrafts in the CBL of over 25% (from a little over 6.5 m/s to below 4.75 m/s) as the optical depth increases from 0 to 0.5. Following the method discussed in *Couvreux et al.* [2009], we define a model grid box to be in an updraft whenever the vertical wind speed is more than 1 standard deviation above the layer mean vertical wind speed. Note that the lateral domain average vertical wind speed is small at all levels in the model since there is only a very modest net upward motion due to thermal expansion as the domain average atmosphere warms during the day. By 1700LT, there is a very strong decrease of updraft speed with optical depth, falling by about 80% as the optical depth increases from 0 to 0.5 (Fig. 3c).

The energy involved in CBL turbulent motions is quantified as the turbulence kinetic energy (TKE). The resolved TKE is calculated from the resolved perturbation velocity components, *u'*, *v'*, and *w'* as:

$$TKE_{resolved} = 0.5 \times (\langle u'^2 \rangle + \langle v'^2 \rangle + \langle w'^2 \rangle) \quad (3)$$

The turbulent component is calculated by $\varphi' = \varphi - \langle \varphi \rangle$ at each altitude for each local time, where '$\langle\ \rangle$' indicates horizontal domain averaging and φ can be wind fields *u*, *v*, *w*, pressure, *p,* and potential temperature, θ. The number of lateral model grid points used in the analysis in this paper is large enough to satisfy the ergodic principle that time and spatial averaging yield similar statistical results [*Stull*, 1988]. The TKE used in our analysis is the sum of the resolved TKE (Eqn. 3) and the prognostic unresolved TKE from the SGS/SFS parameterization (see Appendix A). Also note that TKE is defined as an intensive property such that it is not actually an energy but an energy per unit mass of air (units of m^2/s^2 are the same as J/kg).

Fig. 3d shows the mass-weighted average TKE over the CBL depth as a function of local time, while Fig. 3f shows the mass-weighted average TKE at 1700LT as a function of model optical depth. These figures show that the TKE decreases with dust optical depth, similar to the updraft speeds. The maximum TKE value (between 1400LT and 1500LT) decreases by more than a factor of 2 as the optical depth increases from 0 to 0.5. At 1700LT the decline is nearer 90%. This is a much larger fractional decrease than for either the CBL depth or the updraft speed, suggesting that the CBL becomes much less turbulent as the optical depth increases (which is also reflected in the vertical eddy heat flux, not shown). The total turbulent kinetic energy in the CBL can be obtained as the mass *integrated* TKE in units of *Joules per square meter* within the CBL, which we shall henceforth refer to as the TTKE. The TTKE also dramatically decreases with increasing optical depth, reflecting the much lower convective mixing due to the reduced surface-atmosphere temperature

contrast. This marked negative feedback of dust on CBL convection suggests a significant negative feedback between atmospheric dust optical depth and dust lifting from the surface at PBL / CBL length scales, and its effect is noted in numerical models that parameterize the PBL [*Newman et al.*, 2002].

Fig. 3g and 3i show the evolution of the surface wind drag velocity with local time and optical depth, where the drag velocity, u^*, is related to the shear stress, σ_{stress}, of the wind acting on the surface by:

$$\sigma_{stress} = \rho u^{*2} \quad (4)$$

Where ρ is the air density at the surface. The plots show that the mean, standard deviation and maximum wind all decrease with the increasing optical depth. Since the wind stress is an important contributor to dust lifting, the decrease again suggests a negative feedback between increased optical depth and dust lifting.

4.2 Variable Dust Cases

In order to examine the impact of radiatively-active dust heterogeneity within the CBL while dust is being lifted, we conducted four LES experiments with a single, fixed value of the wind stress lifting threshold (τ^t) but with different lifting rate parameters (α_N) (see Section 2.1 and Eqn. 1). As with the fixed dust cases, all other settings were those from Hinson/Spiga case *i,* (see Section 3 and Table 1) and numerical mesh 3 (Table 3). The dust mass mixing ratio was initialized such that the total visible column depth τ=0.3. The dust was uniformly distributed in the horizontal, and in the vertical the dust was distributed using a Conrath profile (see Section 2). The lifting threshold was tuned so as to allow dust lifting activity to commence as soon as the CBL began to grow at 0800LT. The dust lifting rate parameters for the four simulations were tuned such that the peak dust optical depth in the late afternoon during the simulations fell within increments comparable to those of the

fixed dust cases (τ=0.3–0.4 for the case labeled VD3, τ=0.4–0.5 for case VD4, τ=0.5–0.6 for case VD5 and τ=0.6–0.7 for case VD6). Summary results for the four variable dust cases, are presented in Fig. 2b, 2e, 2h, 2k, 3b, 3e, and 3h. The evolution of the dust optical depth is shown in Figure 4.

Fig. 2b shows the evolution of CBL heights for the four variable dust cases. The CBL heights of all the cases are roughly the same before about 1150 LT but start to differ thereafter. Fig. 2b shows that the maximum CBL height for the VD cases increases with increasing dust optical depth, the opposite of the trend shown in Fig. 2a for the FD cases. Indeed, Fig. 2c shows that between τ=0.3 and τ=0.6, the maximum CBL depth increases from about 7.25 km to about 8.75 km (or about a 20% increase in depth). Directly comparing the FD and VD cases for τ=0.3 and τ=0.5, while the FD cases showed a 22% decrease in CBL depth for the 0.2 increase in increasing optical depth, the VD cases showed an increase in optical depth of about 7% (Fig. 2c).

Fig. 2e and 2h show that the VD cases have a very slightly reduced sensitivity of the surface temperature and the mixed layer potential temperature to the total dust optical depth as compared to the FD cases (also Fig. 2f and 2i). For the ground temperature, the increased optical depth from τ=0.3 to 0.5 produced less than 1 K decrease for the VD case, while for the FD case ground temperature decreased by about 1.5 K (Fig. 2f). For the mixed layer potential temperature, decreased sensitivity to optical depth increase is also apparent (Fig. 2i). Thus, the dramatic change in the magnitude and sign of the change of the CBL depth for a given change of optical depth between FD and VD cases is not controlled by a significant change in the spatial average boundary forcing (*i.e.*, the surface-atmosphere temperature contrast) nor the mean atmospheric static stability (Fig. 2j, 2k, and 2l). While the surface-atmosphere temperature contrasts are larger in the VD cases (Fig. 2l), they do not change with optical depth with the same sign as does the CBL height (Fig. 2c).

Fig. 3b and 3e show the domain average updraft velocity and the mass-weighted TKE within the mixed layer, respectively, for the VD cases. Throughout the development of the CBL, from roughly 0800LT to about 1430LT, both the updraft velocity and the TKE show a weak trend with increasing optical depth. While by 1430 LT, the CBL depth is already 1 km higher for VD6 than for VD3 (7.5 km vs. 6.5 km: an increase of 15% for a doubling of optical depth). In the mature CBL after 1430LT, both the updraft speeds and TKE fall rapidly with local time. By late afternoon (1700LT), the updraft speeds and TKE both also fall rapidly with optical depth (Fig. 3c and 3f). The trends before 1430LT suggest that unlike for the FD cases (*c.f.*, Fig. 3a *vs*. Fig. 3b and Fig. 3d *vs*. Fig. 3e), the vigor of CBL turbulence is largely insensitive to the dust optical depth (for the intermediate optical depths examined) during the period of free convection onset and the strongest thermal forcing. Since the TKE is nearly insensitive to the optical depth and the CBL depth increases significantly with increasing optical depth, more TTKE is involved in thermal turbulence as the optical depth increases. The insensitivity of the updraft speed and TKE to optical depth, and the increase in total CBL TTKE with increasing optical depth suggest that the inhomogeneous dust cases have more energy flowing into CBL turbulence as the dust optical depth increases, whereas the energy flowing into CBL turbulence strongly decreases with increasing optical depth in the FD cases. This in turn suggests that the dust inhomogeneity has an impact that is sufficient to more than offset the effect of shading of the surface.

Before examining variable dust in the LES in more detail, it is useful to take a closer look at how the dust optical depth is changing in these simulations and to provide a quantification for the inhomogeneity of the dust. As described in Section 2, dust is injected at the surface based on the surface wind stress, transported/mixed by resolved winds and diffusively mixed by the SGS/SFS eddy parameterization, and it is. As such, the dust

optical depth changes over time in the simulations. The evolution of the domain average optical depth is shown in Fig. 4 as the solid lines. For all cases, the average optical depth increases over the course of the day. Also shown in Fig. 4 as the dotted lines are the domain minimum and maximum optical depth in any given column. For VD6, the differences in column optical depth can be quite dramatic: *e.g.*, at 1400LT the minimum optical depth is less then 0.4 while the maximum is almost 0.7. The differences between the maximum and minimum column dust opacity for the four cases (VD3, VD4, VD5, and VD6) are ~0.04, ~0.15, ~0.25 and ~0.4 at 1430LT. In all cases, the homogeneity increases after about 1430LT as the TKE and updraft speeds decrease (*c.f.*, Fig. 3b and 3e). In order to more conveniently compare cases with different lateral dust inhomogeneity, we have defined a Dust Inhomogeneity Index (DII):

$$DII = \frac{\sigma}{\tau_{avg}} \tag{5}$$

Where σ is the standard deviation of the column dust optical depth over the whole domain at a given time, and τ_{avg} is the corresponding average optical depth. The DII is shown as the dashed lines in Fig. 4 (but note the offset of 0.3 in order to use the same y-axis as the optical depth). The DII grows as the CBL TKE increases and as the CBL develops stronger vertical plumes, reaching peak values of 0.02, 0.05, 0.08 and 0.1 at 1400LT. The DII then falls as CBL mixing strength and the rate of dust lifting from the surface (not shown) decrease. This trend reflects the increasing concentration of freshly mixed dust into increasingly strong plumes during the morning and early afternoon development of the CBL followed by the lateral mixing and diffusion of this dust in the latter afternoon.

5. Feedback Between Dust Inhomogeneity and CBL Dynamics

The simulations described in Section 4 show that the presence of laterally inhomogeneous dust significantly modifies the CBL compared to simulations with similar total optical

depths but with the dust uniformly distributed. In this section, we take a closer look at one of these cases to examine how the dust is distributed in the variable dust cases relative to CBL dynamical structures, how the CBL large eddy structures are modified, how the presence of the variable dust changes the radiative heating rates, and how these radiative heating rate changes modify the CBL TKE budgets.

In order to more closely compare the fixed and variable dust LES, in this section we show results from the fixed dust scenario case FD5 and the variable dust scenario case VD6 at 1330 LT. At this local time, both simulations have the same total optical depth (and the same top-of-atmosphere insolation), and the DII for the variable dust scenario is at its maximum (Fig. 4). This specific example pairing is shown for illustrative purposes, but similarly controlled comparisons at different local times during CBL development and for different total optical depths exhibit similar qualitative behavior to that described here.

5.1 CBL Large Eddy Structures in Fixed and Variable Dust Cases

Figure 5 shows the full lateral extent of the LES domains for the FD5 and VD6 cases, with Fig. 5a and b showing the perturbation pressure at about 70m above the surface. The relatively thin, green-to-blue regions in these plots indicate the convergence zones at the base of the CBL quasi-cellular convection, while the redder areas indicate higher pressure. The black vectors illustrate the lateral wind field at 70 m altitude, showing flow converging toward these low-pressure lines and diverging away from the high-pressure centers. The black contours on these plots show the coincident locations of the cellular updrafts above the low-pressure lines (the contours in Fig. 5 are the vertical updraft speeds at 2 km). The significantly larger range of the perturbation pressure values in Fig. 5b *vs.* 5a, the generally larger wind vectors (whose length indicates wind speed), and the tighter definition of the updraft speed contours, all suggest the large eddy cellular convection is significantly more vigorous in VD6 *vs.* FD5. This more vigorous convection is also associated with a larger

scale of the Bénard-like convection cell structures (illustrated by the greater depth of the CBL).

The increased vigor of the cellular convection apparent in Fig. 5b *vs.* 5a is directly related to the higher perturbation potential temperatures within the low-pressure regions of the cells. The perturbation potential temperatures at roughly 70m (Fig. 5c and 5d) show a greater fraction of the low-pressure cell boundary having higher perturbation potential temperatures and a larger area of peak values in the VD6 case *vs*. FD5. In turn, the higher peak potential temperatures are associated with high total column optical depths (Fig. 5e and 5f). While both cases have the same domain average optical depth (0.5), the VD6 case has peak dust optical depths aligned along the convergent, upwelling walls of the cellular convection, with peak values up to 0.7, while in the broader downwelling and divergent high-pressure cellular centers, the atmosphere is relatively clearer with optical depths as low as 0.35.

The effect of the cellular convection in concentrating dust into the upwelling walls of the cell is even better illustrated in Figure 6, which shows lateral (x-z axis) slices from FD5 and VD6 along the white lines indicated on Figure 5. In Fig. 6a, the imposed incremental optical depth is by definition uncorrelated with the vertical cellular motions, which are illustrated with the black vectors. The significant concentration of the incremental dust optical depth in the large eddy convection cell in the VD6 is very clearly evident in Fig. 6b. An instantaneous snapshot of the dust mass mixing ratio behind the optical depth distribution provides an even clearer indication of the connection between the convection cell and the dust (Fig. 6c). Near the surface, the wind both lifts dust into the atmosphere (due to the wind stress lifting parameterization, Section 2) and concentrates this dust into the base of the upwelling plumes along the convergence zones of the cells. The dust then rises with the thermals in the updraft areas. Indeed, at this local time, the mean CBL depth

in VD6 is 6.5km, and thus Fig. 6c shows that some of the dust can rise all the way up to the top of the CBL and overshoot into the free atmosphere above. In reaching the upper part of the CBL, the air begins to diverge and then to subside. The dust is laterally spread in the upper CBL by these divergent winds and is mixed with the air in the subsiding portion of the CBL under the influence of smaller scale resolved and SGS/SFS unresolved turbulence. During the period of strongest development of the CBL, the lofting and entrainment of dust within the upwelling zones is more efficient than the lateral mixing, and very significant (factor of 4-5) lateral contrasts of dust mass mixing ratio can develop within the lowest few 100m of the CBL (Fig. 6c).

The degree of dust concentration within the large eddy updrafts can be statistically evaluated by performing a correlation analysis between perturbation dust mass mixing ratio and the perturbation vertical wind speed for each point in the horizontal domain, at each altitude, and for each local time. Figure 7 shows the variation of this correlation index with local time and altitude for the VD6 case. We can see that the correlation region with index values larger than 0.5 grows with the CBL height until 1500 LT, after which it begins to decrease. This corresponds to the evolution of the DII shown in Figure 4, which also starts to fall after 1500 LT. Figure 7 demonstrates that throughout the domain dust tends to concentrate in the updrafts during the entire growth period of the CBL.

5.2 Direct Radiative-Dynamical Feedback Associated with Inhomogeneous Dust Radiative Heating

The Martian CBL is a radiatively dominated environment due to the low atmospheric density and heat capacity [*Gierasch and Goody*, 1968; *Micheals and Rafkin*, 2004; *Spiga et al.*, 2010]. Unlike the Earth, the sensible heat flux from the surface and the latent heat due to water exchange are negligible compared to the radiative heating in the energy budget

of the Martian CBL. Hence, radiative-dynamical feedbacks due to the kind of dynamical concentration of dust described in Section 5.1 could be significant in the CBL.

In order to quantitatively illustrate the importance of radiative heating due to dust inhomogeneity, Figure 8 shows the total visible heating rate at roughly 1 km above the surface and at 1330 LT for both the FD5 and VD6 cases. Since the visible heating is due almost exclusively to dust absorption, the FD5 case (Fig. 8a) shows essentially no lateral variations, with a heating rate of about 1.75K/h. The VD6 case (Fig. 8b), on the other hand, shows significant variations in the heating rate consistent with the large variations in optical depth (Fig. 5f). The heating rate varies from about 1.6K/h to about 3.5K/h, thus yielding a peak heating rate in the domain at this level and local time that is about a factor of 3 higher than the minimum heating rate (*i.e.*, these exists a maximum lateral horizontal heating contrast of about 2K/h or a factor of 3 in total magnitude). The heating maxima and minima occur in close association with the perturbation potential temperatures in Fig. 8b, again showing that the lateral dust distribution (which controls the visible heating rate) is strongly correlated with the warm upwelling plumes/sheets of the large eddy CBL convection.

Cross sections of the visible, infrared, and total heating rates through the domains shown in Figure 9 (these cross sections are at the locations indicated on Figure 8 by the white horizontal lines). The FD5 case illustrates some general features of the lower atmospheric energy budget. With a nearly uniform horizontal and vertical distribution of dust opacity, and only a very minimal amount of solar absorption by atmospheric gases, the visible heating rate is also rather uniform. By contrast, the infrared heating rate is dominated by the strong net absorption of the upwelling infrared radiation from the surface by the cooler atmospheric CO_2 in the lowest reaches of the CBL [*Geirasch and Goody*, 1968; *Savijarvi*, 1999; 2004]. During this portion of the day (1330 LT), the net heating rate shows the rapidly vertically decaying signature of the infrared heating by absorption of surface

radiation within the lowest 1-2 km, superposed on the much more vertically uniform and weaker solar heating of suspended dust (Figs. 9a, 9c, and 9e).

The presence of dust concentration in the plumes is illustrated by the structure in the visible heating rate from the VD6 case (Fig. 9b). The visible heating rate also dominates the total heating rate above about 500m-1km (Fig. 9f). Here, there is significant enhanced solar heating within the thermal plumes, generating the factor of 3 difference between the upwelling thermal plume core and the downwelling zone mentioned previously at the roughly 1km level. As with the horizontal slices through the model (comparing Fig. 8b and Fig. 5f), the large values of the visible heating rate are highly correlated with large values of the dust mass mixing ratio in vertical cross section, and vice versa (Fig. 9b *vs.* Fig. 6c).

The lateral differences in heating rates are only of consequence if they generate a significant augmentation of the potential temperature differences between the upwelling versus the downwelling portions of the convection cells. This efficacy depends not only on the heating rate but also the length of time that the air spends in the region experiencing the excess heating, which in turn depends upon the overturning timescales of the large eddies. We can estimate the uplift timescale from the CBL vertical scale, W^*, modified from its traditional form [*e.g., Stull*, 1988] by *Spiga et al.* [2010] (this is the modified Deardorff velocity):

$$W_* = \left[g z_t \frac{\langle w'\theta' \rangle_{max}}{\langle \theta \rangle} \right]^{1/3} \quad (6)$$

Where z_t is the CBL top height, $\langle w'\theta' \rangle_{max}$ is the maximum buoyancy flux (where primes indicate the perturbation from the horizontal average), and $\langle \theta \rangle$ is the domain average mixed layer potential temperature. Taking the *Spiga et al*. [2010] value of 4-6.5m/s, the time it

takes for air to cycle from the surface to the top of the CBL (about 6km in this case) is about 20 minutes. For a heating rate contrast between the warm and cool branches of the large eddy cell of about 2K/h, this yields about a 0.67K lateral contrast due solely to the differences in visible radiative heating rates in the upwelling and downwelling thermals. The 0.67K can be compared against the observed potential temperatures in Fig. 5d and Fig. 9b, 9d, and 9f. Above about 1km, most of the positive potential temperature perturbation is clearly associated with the visible dust heating. The reduction of the thermal contrasts in the upper portion of the plumes is due to mixing (entrainment) between air in the thermal plume and the background atmosphere.

The warming of the updrafts increases their positive buoyancy which leads to a strengthening of the vertical motions in the CBL. Figure 10 shows the vertical wind speed distribution (the number of grid cells at a given level within a given vertical wind speed bin) as a function of altitude and vertical wind speed bin. The vertical discretization in Fig. 10 corresponds to the model vertical mesh, while the vertical wind speed binning has a bin size of 1m/s. Both the FD5 (Fig. 10a) and VD6 (Fig. 10b) cases are shown for 1330LT. Both panels show that the vertical wind is generally small near the surface, where buoyancy has not yet had chance to vertically accelerate the air, and in the free atmosphere above the CBL top. Within the interior of the CBL, the vertical wind speed extremes correspond to the upwelling plumes and the downwelling zones of the convection cells. The largest vertical wind speed magnitudes appear within the upwelling plumes in the upper part of the CBL. In Fig. 10, the maximum values are 17 m/s for FD5 and 18 m/s for VD6.

Fig. 10c shows the relative difference between the two simulations and demonstrates a greater occurrence of higher wind speed magnitudes of both signs in the VD6 case versus the fixed dust FD5 case. Specifically, wind speeds larger than +10 m/s (upward) and less than -5m/s (downwards) are more prevalent in VD6 than FD5 at most altitudes, suggesting

that both the updraft and downdraft are stronger in the variable dust case. Specifically, we can see a significant difference in the upward wind between 1-2km altitude, corresponding to the maximum VD6 dust visible heating rates in the updrafts shown in Fig. 9b. The large difference at 4-6km, however, is due to the difference of the CBL heights between the two cases (~6km for VD6 but ~5 km for FD5). The lateral domain average vertical wind speed of the updrafts for VD6 is also much larger than that for FD5 at all altitudes.

Stronger vertical motion in the VD6 up- and downdrafts must be supported by more rapid horizontal motions near the base and tops of the large eddies. This is indeed illustrated by the frequency spectrum of horizontal wind speed shown in Figure 11. The larger horizontal wind speeds for VD6 suggests that the whole Bénard-like convection cell circulation is enhanced. The higher frequency of occurrence of large horizontal wind speeds near the surface (8–13m/s as shown in Fig. 11c) suggests that more dust maybe lifted and concentrated into updrafts when radiatively-interactive dust is treated. This would create a positive feedback for the dust lifting process, but it is strictly the wind stress at the surface that is important for dust lifting rather than just the wind speed, and we will return to this issue in the discussion section. It should also be noted that as a background wind is applied, the convection tends to change from polygonal Bénard cells into convective roll (or street) structures. These rolls have greater anisotropy than Bénard cells and hence high rates of turbulent mixing [*e.g., Stull* 1988], and thus the feedback on dust lifting may have even greater potential when there is a background wind in which the convection is embedded.

5.3 Indirect Radiative-Dynamical Feedback Associated with Surface Shading

Figure 12 shows the lateral distribution of the ground and lowest layer air potential temperatures in the FD5 and VD6 cases at 1330LT. While the lateral average ground temperature is very slightly cooler in FD5 (268.1K) versus VD6 (268.4K), comparison of Fig. 12a and 12b shows that there is a much greater variation within VD6 (about 1.4K

variation versus about 0.8K for FD5). Specifically, the areas of enhanced ground temperature in VD6 are under the downwelling regions of the open cellular convection. The excess thermal emission from the surface in the downwelling regions of VD6 versus FD5 is thus about 1% and given that most of the atmospheric heating in the lowest ~500m of the atmosphere is due to thermal infrared radiative exchange with the surface, this corresponds to an augmentation of lowest layer atmospheric heating by this same factor. Within the convection cell, this corresponds to augmented surface-to-atmosphere exchange of heat in VD6 versus FD5, despite the fact that the lateral domain average dust optical depths and the resulting lateral domain average ground temperatures are nearly identical.

The reason that augmented ground temperatures occur under the downwelling centers of the convection cells in VD6 (*vs*. FD5) is that these regions are relatively clear of dust (Fig. 5f). The relative concentration of dust in the upwelling plumes means that for the domain average optical depth in VD6 to equal that in FD5 (τ=0.5), there must be a lower dust optical depth in the downwelling regions. Indeed, above the area of maximum ground temperature, the optical depth is as low as 0.35. Since the clearer downwelling regions have higher ground temperature and hence higher rates of near-surface atmospheric heating, the dust inhomogeneity generates a separate, secondary means of augmenting the thermal forcing of convection (in addition to direct heating of the dusty upwelling plumes, Section 5.2). The reason that the heating augments the circulation despite being under the downwelling regions is due to the fact that surface-atmosphere thermal infrared heat exchange is predominantly short range, and thus only significantly heats the lowest portion of the CBL (*e.g.*, Fig. 9d). Within this very lowest portion of the atmosphere, the air is strongly divergent away from the downwelling zones and convergent into the upwelling cellular edge sheets and plumes. The extra buoyancy deposited into the air due to the heating is thus advected into the upwelling zones where it enhances the cellular overturning. This lateral advection of buoyancy happens sufficiently quickly that vertical propagation

of the buoyancy within the downwelling zone is overwhelmed, otherwise the heating distribution would instead act to slow the downwelling.

5.4 Efficiency of Surface-Atmosphere Heat Transfer

The lowest atmospheric layer domain average potential temperature in the FD5 is significantly higher (235.5K) versus that in the VD6 case (232.2K) at 1330LT (Fig. 12c and 12d, respectively), despite VD6 having a very slightly higher ground temperature (the potential temperature difference is +3.3K while the ground temperature difference is -0.3K; Note also that potential temperature is calculated using P_0=610Pa in this paper). The relative coolness of the VD6 near surface air is qualitatively what one would expect given the stronger convective motions (more vigorous overturning and faster near surface winds) in the variable dust case (*i.e.*, VD6 is less stable than FD5). With more vigorous motion, the VD6 Bénard-like cells are able to more effectively ventilate cool air down into the near surface divergence zones, and the air spends less time traveling horizontally within the near surface portion of the cell and thus has less time to absorb heat (mostly in the form of infrared heating) from the surface.

The difference between the surface temperature and the kinetic temperature of the lowest layer of the model is thus larger the VD6 case (34.3K *vs.* 30.7K for FD5, note that the Exner function value in the lowest model layer for Hinson/Spiga *case i* simulations like FD5 and VD6 is 1.008098—where the Exner function, Π, is defined such that $T=\Pi\theta$, where T is the kinetic temperature and θ is the potential temperature). This is about a 12% larger surface/atmosphere temperature contrast in the VD6 case than in FD5. The surface/atmosphere heat exchange is dominated by sensible and infrared heat exchange between these layers and for a given pressure, composition, and mean temperature, both depend strongly on the temperature difference. As such, the enhanced overturning of the cell driven by the direct heating of concentrated dust in the upwelling plumes (Section 5.2)

and secondarily by the greater ground temperatures beneath the downwelling portions of the cell (Section 5.3), leads to cooler air over the surface and thus allows the cell to extract more energy from the surface. To be precise, the same energy is emitted from the surface (over the course of the simulations, the domain mean ground temperatures do not diverge significantly between FD5 and VD6), but more of this energy is deposited into the cellular motion in VD6. Inhomogeneous dust thus allows the CBL to convert more of the surface emission into turbulent kinetic energy.

The domain average modified Deardorff velocity, W^* (see Eqn. 6 and Section 5.2) for all the FD and VD cases is shown in Fig. 13a and b as a function of local time, and in Fig. 13c as a function of optical depth at 1700LT. These can be referenced to the difference between the surface temperature and the kinetic temperature of the lowest model layer shown in Fig. 2j, 2k, and 2l. In these simulations, the surface-atmosphere temperature contrast is a good proxy for the net heat exchange between the surface and the atmosphere, dominated as it is by infrared heating of the atmosphere by surface emission. Since all of the VD cases begin from an initial τ=0.3 state and that significant differences in optical depth do not develop until the late morning (after lifting has progressed), there are no differences in the surface/atmosphere temperature contrast evolution until just before noon (Fig. 2k). This differs from the FD cases where optical depth differences through the night and morning yield a steady-state shift of the diurnal surface temperature cycle to a lower mean value and hence decreases the surface/atmosphere temperature contrast throughout the interval shown in Fig. 2j. Once the increased optical depths start to influence the VD surface/atmosphere temperature contrasts after noon, the sign of the dependence on optical depth is the same of that as for FD, namely that the contrast decreases as the optical depth increases (Fig. 2l).

The CBL velocity scale, W^*, decreases as the surface/atmosphere temperature contrast decreases for the FD cases (Fig. 13a and 13c, *vs*. Fig. 2j and 2l). This suggests that as the near-surface forcing decreases the vigor of convection also decreases, as we might expect. Comparing with Fig. 2a, both the modified Deardorff velocity, W^*, and the CBL height decrease with increasing optical depth (and hence decreasing surface/atmosphere temperature contrast). This is consistent with the idea that stronger forcing for thermal turbulence (in this case, near surface forcing) should lead to stronger vertical CBL motions and a deeper CBL.

However, Fig. 13b shows a striking lack of sensitivity of the modified Deardorff velocity to the optical depth in the VD cases until early afternoon. A significant part of this seems likely traceable to the similarly striking insensitivity of the surface/atmosphere temperature contrast to dust optical depth for the VD cases (Fig. 2k). In turn, part of this is due to the fact that the optical depth only begins to differ between the VD cases in the mid-to-late morning. However, W^* remains insensitive to the optical differences into the mid-afternoon (1430-1500LT), at which time it starts to show the same sign of sensitivity as the FD cases, namely decreasing W^* with increasing optical depth (and decreasing surface/atmosphere temperature contrast). The fact that W^* has nearly identical trends with local time in the VD cases up to about 1500LT despite differences in the total optical depth suggests that increasing optical depth (*i.e.*, the lifting of dust at increasing rates) does not actually increase the vigor of the turbulence despite increasing the CBL depth. However, it must be cautioned that even the modified Deardorff velocity is defined assuming that the total heat input into the turbulence is based on heat transfer from the surface (the modification simply relaxes the traditional assumption that this heat is predominated injected by the sensible heat flux from the surface). When significant buoyancy is being added through visible radiative heating of the suspended dust in laterally inhomogeneous plumes, even the modified Deardorff velocity would decreasingly capture the true vigor of

CBL turbulence. In this case, the turbulence is no longer free thermal convection, but has a forced component (the differential heating due to the dust) which becomes analogous in some ways—at least in terms of it not being pure, free thermal convection—to moist convection.

5.5 Vertical Dust Distribution Differences Associated with Active Dust Lifting

The evolution of the domain average vertical potential temperature structure as a function of local time is shown for FD5 and VD6 in Figure 14. Comparing the two panels, Fig. 14 clearly demonstrates the deeper extent and more rapid growth of the CBL in VD6. In both cases, the CBL depth can be estimated by finding the point in altitude where the isentropes are no longer nearly vertical (very near the surface, the isentropes transition to being nearly vertical from being nearly horizontal—this altitude, which illustrates the top of the superadiabatic layer, should not be confused with the higher-altitude CBL top). The thermal structure signatures of the CBL top are the basis for the FD5 and VD6 CBL depth curves in Fig. 2a and 3a, respectively.

As well as being deeper than the FD5 CBL, the VD6 CBL is also cooler throughout its depth. This is consistent with the cooler near surface air temperatures discussed in Section 5.4. Despite the mean potential temperature in the CBL being slightly cooler in VD6, the difference between the updraft and downdraft potential temperatures in each simulation are quite similar (Figure 15).

At levels above the CBL, FD5 is warmer than VD6. This is attributable to the fact that the vertical distribution of dust prescribed in FD5 is more nearly vertically uniform than in VD6 (Fig. 6a and 6b), which means that the heating of the atmosphere (primarily due to solar absorption by dust) is also greater above the CBL top in FD5 *vs*. VD6 (Fig. 9a and 9b). The difference in heating rates above the CBL at 1330LT is about 0.7K/h (Fig. 9e *vs*. f).

5.6 Dependence of CBL Turbulence on Optical Depth and Local Time

Figure 16 shows the dependence of the surface-air temperature contrast, the CBL height, the surface drag velocity, the modified Deardorff velocity, and the average CBL TKE upon the domain-average optical depth at 1330LT and 1500LT. These plots complement Fig. 2l, 2c, 3i, 13c, and 3f, respectively, which show these values at 1700LT. The DII for the VD cases decreases from a maximum at 1330LT to nearly zero for all the VD cases at 1700LT (see Fig. 4).

The surface-atmosphere temperature dependences upon optical depth at 1330LT and 1500LT (Fig. 16a and 16b) both show the same sign of trend as at 1700LT (Fig. 2l), with an increasing optical depth yielding a decreasing thermal contrast for both the FD and VD cases. However, the offset of the VD curves towards higher thermal contrast values for VD versus FD for the same optical depths is largest at the earliest local time and smallest at the latest local time. This is consistent with the difference in surface-atmosphere temperature being due to the dust inhomogeneity discussed in Section 5.3 and 5.4, given that the DII decreases with time after 1330LT (Fig. 4). The residual differences between FD and VD contrasts at 1700LT result from the differences in the time history of heating in the two sets of cases.

The CBL height trend with optical depth is consistent at all three local times (Fig. 16c, 16d, and 2c). While across the FD cases, CBL depth decreases significantly with increasing optical depth, a strongly opposite trend is apparent at all three local times for the VD cases. The trend at 1700LT cannot be explained as a purely historical signature of earlier gains in CBL depth as the CBL is clearly still growing through to the end of this period, at least in the VD5 and VD6 cases.

While the drag velocity (u^*) appears to have no difference in behavior with increasing optical depth in the VD and FD cases at 1700LT (Fig. 3i), this is not the case at the earlier local times. In the midafternoon (1500LT, Fig. 16f), while the mean drag velocity shows no difference between FD and VD, there is a very slight separation of trend in the one sigma deviation winds, and a noticeably higher maximum drag velocity in the VD versus the FD cases. At the time of peak DII (1330LT, Fig. 16e), all three measures of the drag velocity are higher for the VD cases versus the FD cases. Thus, for the same domain average optical depth, dust inhomogeneity significantly increases both the mean and extremum values of the drag velocity. The VD cases also do not show any meaningful trend with optical depth at this earlier local time, unlike the FD cases at this local time and the FD and VD cases at the later local times. This suggests that the negative feedback of increasing dust optical depth upon free convective wind stress generated dust lifting apparent in the FD cases is not active when dust is most inhomogeneously distributed.

The modified Deardorff velocity (W^*) shows a change in trend with optical depth for the three local times examined (Fig. 16g, 16h, and 13c). At the earliest local time, while for the FD cases W^* decreases as the optical depth increases, consistent with the surface shading resulting in a reduction in vigor of the CBL turbulence, the VD cases show a 5% increase in W^* with optical depth increasing from 0.3 to 0.5. At 1500LT, the trend for the FD case is similar to that at 1330LT, but the VD cases are nearly independent of total optical depth (W^* arguably increases very slightly to about 0.5 optical depth and the decreases slightly above that). By 1700LT, the VD case W^* decreases with increasing optical depth, though at a slightly lower rate than the FD cases. These results suggest that when the DII is largest (and solar forcing the strongest), the vigor of CBL turbulence as diagnosed by W^* increases as more dust is placed in the atmosphere.

5.7 Modification of the TKE Budget Due to Inhomogeneous Dust Radiative Heating

The evolution of TKE is expected to follow the TKE tendency equation (written here following Eqn. 5.1b from Stull [1988]):

$$\frac{\partial(\langle TKE\rangle)}{\partial t} = \frac{g}{\langle\theta\rangle}\langle w'\theta'\rangle - \langle u'w'\rangle\frac{\partial\langle U\rangle}{\partial z} - \frac{\partial\langle w'.TKE\rangle}{\partial z} - \frac{1}{\langle\rho\rangle}\frac{\partial\langle w'p'\rangle}{\partial z} - \varepsilon \quad (7)$$

The tendency equation says that the TKE at any level ought to evolve following the five terms on the right hand side of Eqn. 7, which are respectively, along with one letter labels we will use for these terms: (B) The buoyant production/consumption term (which depending on whether the vertical heat flux $\langle w'\theta'\rangle$ is positive or negative); (S) The mechanical or shear production term; (T) The turbulent transport of TKE term; and, (P) The pressure correlation term. As we are interested in the mechanisms by which TKE is generated, we have not calculated the dissipation, ε, which is the rate at which TKE is converted into thermal energy. Indeed, for steady state LES, ε is usually calculated as the residual of the other terms necessary to have no net trend in TKE. With an evolving CBL (as in our simulations), it would be calculated from the model evolution of total TKE minus the sum B+S+T+P. It should be noted, however, that the functional form of turbulent dissipation is related to the deformation of the turbulent wind field and hence is inversely proportional to the length scale of the turbulent motions.

Figure 17 shows the vertical structure of the terms B, S, T, and P for FD5 and VD6 calculated over the period of growth of the CBL. The relative trends and values of the terms compares very well with LES, convection tanks, and terrestrial field observations for strongly buoyantly driven turbulence (free convection), which can be seen by comparing Fig. 16 with (*e.g.*) Figure 5 from *Moeng and Wyngaard* [1989] and Figure 11 from *Moeng and Sullivan* [1994]. Specifically, Fig. 17 shows that TKE in the lower CBL is generated by a combination of buoyancy generation (B) and the pressure correlation term (P), with the turbulent transport term (T) acting to reduce the TKE (*i.e.*, by upward transport of the

TKE). In the upper half of the CBL (*i.e.*, for $z/z_{top}>0.5$), B continues to decrease and becomes negative in the overshoot region just above the CBL top. Through the depth of the CBL, the T and P terms are anticorrelated, with the zero crossing of both occurring at about the $z/z_{top}=0.5$ level. Thus, the vertical variation of TKE shows a significant net source of TKE in the lower CBL both from B and P, a net upward vertical transport of TKE by eddy motions (T), and finally a net sink of TKE in the upper CBL due to P as eddies are damped through interaction with the overlaying statically stable free atmosphere. Fig. 17 shows that both the fixed and variable dust simulations are in the limit regime of free convection regime during the daytime (output were averaged from 0900-1600LT), since the shear term (S) is negligible compared to the other terms. It also shows that the TKE vertical budgets, in both cases, have no major differences from those observed and modeled for the Earth during free convection [*Moeng and Wyngaard*, 1989; *Moeng and Sullivan*, 1994].

The value of TKE as a function of depth in the CBL is shown for both FD5 and VD6 at 1330LT in Figure 18a. In both cases, the TKE is nearly constant with height up to about $z/z_{top}=0.8$ (due to the efficiency of turbulent mixing, term T, Fig. 17), above which it decreases rapidly (due to the damping influence of the P term, Fig. 17). However, Fig. 18a shows that the absolute value of the TKE is much larger in the variable dust, VD6 case, with a peak value of about 16 m^2/s^2, while the fixed dust, FD5, exhibits a peak value nearer 11 m^2/s^2. There is thus about 45% more TKE within the VD6 CBL, and the factor is even higher when the influence of the higher CBL top in VD6 is also considered (*i.e.*, when the TTKE in *Joules/m*^{2} is considered rather than intensive TKE in *Joules/kg* = m^2/s^2). This confirms the analysis from Sections 5.2-5.4 that shows that more total energy is introduced into CBL motions when the dust distribution is inhomogeneous, even while the total dust optical depth remains similar.

Fig.18b shows the vertical heat flux for both FD5 and VD6 at 1330LT. While VD6 has a larger maximum to minimum range of heat flux (a change of 2.4Km/s *vs*. 1.2Km/s) the depth of the CBL is also significantly deeper for VD6 such that the dynamical heating rate (due to the vertical flux divergence in K/s) is much more similar in the two cases. It should be noted that since the VD6 CBL contains more total mass than the FD5 CBL, the total dynamical cooling rate in terms of energy is larger for VD6. Thus, the more vigorous VD6 CBL turbulence (in terms of total TKE) indeed yields a more effective CBL dynamical cooling (in terms of energy per unit column of atmosphere per unit time). The relative vigor of the VD6 CBL versus that of FD5 is also illustrated in Fig. 18c, which shows the average updraft speeds in VD6 are as much as 27% larger than in FD5.

The individual terms of the TKE budget Eqn. 13 are shown in Figure 19, which is analogous to Fig. 17 except in Fig. 19 only output from 1330LT is shown, and the components are rescaled on their own panels for clarity. As in Fig. 17, we see that the buoyant production (B), pressure correlation (P), and the turbulent transport (T) are comparable in magnitude, while the shear or mechanical production (S) term is always negligible and thus at 1330LT both cases are in the free convective regime. Fig. 18a shows that for VD6 the buoyant production of TKE is much larger than that in FD5 in the lower half of the CBL. The difference between the two cases is very similar to that of the vertical eddy heat flux (Fig. 18b). This is not surprising as the buoyant production can be obtained from the vertical eddy heat flux by multiplying by $g/\langle\theta\rangle$, and where $\langle\theta\rangle$ (the lateral domain average potential temperature) differs by less than 2% between the two cases. Therefore, the difference in the CBL energy budget between the variable and the fixed dust cases is mainly driven by the difference in $\langle w'\theta'\rangle$, which is the quantification of the extra buoyancy introduced by the inhomogeneity of dust when it is allowed to be lifted and self-concentrates into the upwelling plumes. The $\langle w'\theta'\rangle$ is increased in the variable dust case because of the simultaneous enhancement of potential temperature θ due to the extra

visible heating by airborne dust concentrated into the upwelling plumes, and the enhancement of the upwelling wind speed, *w*, of these plumes due to their increased buoyancy.

6. Discussion

6.1 Lateral Dust Inhomogeneity and the Boosting of the Height of Dust Lifting

The most dramatic signature in the VD cases presented in this paper is the strong growth of CBL depth with increasing optical depth and DII (Figure 2). The increase occurs due to the visible radiative heating of dust concentrated into the upwelling sheets and plumes of CBL Bénard-like open cellular convection. These results suggest a significant difference in the behavior of the CBL depth, and specifically the vertical extent of dust mixing when dust is being actively lifted. When dust is being lifted within the "feeding zone" of a CBL Bénard cell (defining a lateral scale of a few kilometers to at most 40km), the cell will take on the character of the VD cases in this paper, where there is a strong positive feedback between dust lifting (increasing dust optical depth and DII) and the depth of vertical mixing of the dust. Conversely, when there is no active dust lifting within a cell, an increase of dust optical depth (due to lateral advection of dust) tends to decrease the CBL depth and hence the depth of dust mixing. Even for moderate optical depths and the same average optical depth over the cell, the difference in the mixing depth between active lifting and no active lifting can be several kilometers.

In reality, the difference is likely to be even larger. As the upwelling plumes ascend, the structure of the vertical motion field becomes increasingly dominated by the strongest plumes, usually those plumes originating from near surface "triple junctions" where cellular walls meet. As a result of the concentration of the upwelling into focused plumes, the plumes generally ascend significantly higher even than the average CBL top. For

example, at 1330LT in VD6, the CBL top is diagnosed to be at 6.4km altitude, while the deepest plumes have injected dust almost up to 8km altitude (or about 1.6km or 25% overshoot, see Fig. 6c and Fig. 16a). The FD case at the same optical depth and local time has a CBL top at 4.9km, thus the plume overshoot is about 65% (or 3.1km) higher than the CBL top with no dust lifting.

These simulations suggest that global models using radiatively and dynamically interactive dust that allow inline PBL schemes to vertically mix the dust are likely substantially underestimating the vertical depth to which surface-lofted dust can be spread [*e.g.*, *Newman and Richardson*, 2015]. Indeed, models using such an approach generally yield vertical thermal profiles that are excessively stable and vertical profiles of dust that exhibit too great of a decline with height compared with observations [*e.g.*, *Lee et al.*, 2011]. The observed transport of dust to high altitudes also includes features with maxima of dust mass mixing ratio away from the surface [*Heavens et al.*, 2010]. The difference of maximum dust penetration heights between active dust lifting and non-active lifting area provides a mechanism for creating layers of dust since the CBL above active areas emplace dust to levels that cannot then be mixed down in later sols when the lifting has stopped, or when the dust has advected into surrounding non-active regions. While the typical CBL depth are not high enough in themselves to explain the observed altitude range of dust layers, when combined with variations in topography and with the "solar escalator" mechanism [*Daerden et al*., 2015] the proposed mechanism for the creation of layers may be important.

6.2 The Sensitivity of CBL Depth and Surface Frictional Velocity to DII

The competing factors damping and augmenting CBL turbulence in the FD and VD simulations are 1) the shading of the surface by increasing dust optical depth causing the surface-atmosphere temperature to decline, and 2) lateral differences in the heating of the surface and atmosphere as dust is concentrated into CBL plumes. In the absence of the

latter, an increase of optical depth leads to a rapid decrease in CBL depth and the energy contained in CBL turbulence. However, this paper has shown that inhomogeneity of dust causes both a significant increase in the depth of CBL mixing and in the vigor of CBL mixing.

It will be important in future work to further explore how the CBL responds to a range of DII and optical depth combinations, which have not been exhaustively explored in this paper due to time and page length limitations. However, an initial pilot exploration of the sensitivity of CBL height and surface frictional velocity is shown in Figure 20. For this pilot, we performed dozens of LES cases with different initial dust optical depths and lifting rate parameters. Even though only a limit range of modest DII values were examined, the CBL depth shows a very clear dependence on DII. Significantly, the importance of the DII increases as the dust optical depth increases, with the CBL depth doubling for a change of DII from 0 to 0.15 when the total domain average visible dust optical depth is 0.5. This suggests that the inhomogeneity feedback becomes increasingly potent as the dust optical depth increases, which has a compounding effect on the feedback. The compounding effect in these simulations occurs after the DII exceeds about 0.125, after which increasing dust optical depth and increasing DII each separately lead to increasing CBL depth.

For the range of dust optical depth and DII considered in this pilot study, the feedback of dust optical depth and DII on frictional velocity (and hence surface wind shear stress) is more muted (Fig. 20b, 20c, and 20d). For DII=0, the frictional velocity dependence on optical depth is intuitive, with the value decreasing with increasing optical depth. However, for all but the smallest optical depths, there is a slight positive trend of mean, one-sigma, and maximum frictional velocity with DII. Above DII=0.15, there is also the hint of a reversal of the dependence of maximum frictional velocity upon total dust optical depth, such that increasing optical depth might begin to yield increased wind stresses. If real, this

would be important as it would suggest that above certain thresholds of optical depth and DII, there might exist a positive feedback for wind stress dust lifting that is intrinsic to the CBL. There is clearly insufficient signal-to-noise in the pilot study output to address this suggestion, and thus here we simply note a tantalizing question that needs to be addressed in a future work.

6.3 Uncertainties Associated with the Vertical Distribution of Dust and Time Evolution

Controlling for differences in the dust vertical structure and hence in heating above the CBL is a tradeoff from the perspectives of both model implementation and the underlying physics one is trying to simulate. From the perspective of model implementation, one must choose between comparing similar total optical depths versus comparing similar free atmosphere visible dust heating. Since the variable dust cases unavoidably involve active dust lifting from the surface, their dust distribution will always tend to be centered lower in the atmosphere than a "steady state" fixed dust case. If the experiments were to be designed in order to obtain similar heating in the free atmosphere, the dust column optical depth in a variable dust case would always be higher. In our comparisons, we have decided to emphasize similar optical depths since these then correspond to similar dust shading of the surface and to similar total visible dust heating of the atmosphere.

Moreover, since dust lifting is always from the *surface*, it is a real physical effect that the vertical dust distribution will always be more steeply concentrated at the surface in this case rather than in an atmosphere where no lifting occurs. When no lifting is ongoing, dust will be well mixed to the daytime maximum CBL top or will even increase in layers well above the area average CBL top [Heavens *et al*., 2011]. Therefore, the unavoidable differences in the vertical gradients of visible dust heating evident in Fig. 9a and 9b are an additional way in which the processes responsible for laterally inhomogeneous dust (*i.e*., dust lifting and entrainment in CBL plumes) augment the strength of the CBL compared

to a fixed dust case. The more bottom-heavy dust distribution in a CBL where dust is being actively lifted generates more heating in the lower portion of the CBL and less heating in the free atmosphere into which the CBL grows, and thus increases buoyancy relative to the fixed dust case.

6.4 Parameterization of PBL Properties for GCM and Mesoscale Models

Most of our focus in the discussion section so far has been on how inhomogeneous dust impacts the dust vertical distribution and dust lifting. However, these facets of the discussion rely on the primary result of this paper that the CBL dynamics are fundamentally modified by the dust inhomogeneity radiative effects compared to cases with uniform dust. The inhomogeneity is only important in areas of active dust lifting. While the area of the planet involved in active dust lifting at any given time associated with local dust storms and dust devil activity is likely to be small [*e.g., Cantor et al.,* 2001*; Fisher et al.,* 2005], it is possible that the significant differences in the CBL in these locations might influence globally integrated heat, momentum, and water exchange with the atmosphere. Current PBL parameterizations in models that do not resolve the PBL do not include any representation of the effects of dust inhomogeneity on the CBL. Indeed, the influence of dust inhomogeneity upon predicted CBL heights suggests that there is likely need to revisit modeling of radio occultation-derived CBL height [*Hinson et al.,* 2008*; Spiga et al.,* 2010]. Specifically, for the Hinson/Spiga case i, when using uniform dust both the present model and the *Spiga et al.,* [2010] LES underpredicted the observationally estimated CBL depth by about 2.5km (see Table 2). However, for different combinations of dust loading and DII, the MarsWRF LES can plausibly match the observationally estimated CBL depth (Fig. 2a and 20a). A more focused study looking specifically at the plausible optical depths and DII for each radio occultation profile would be needed to fully explore the DII effect in resolving discrepancies between extant LES predictions and radio occultation retrievals.

The LES output from this study will provide a resource from which a PBL parameterization that includes dust inhomogeneity could be developed. An attractive method of parameterization is the Eddy Diffusion / Mass Flux (EDMF) approach [*Siebesma and Teixeira*, 2000; *Siebesma et al.*, 2007] in which the PBL motions are described in terms of the simultaneous effects of a local background eddy diffusion (ED) and a nonlocal mixing by deep plumes using a mass flux (MF) representation. The parameterizations are built by constraining the relationship between the mass and heat tendencies output from the MF scheme and the input resolved thermal and wind structure using the plume behaviors from LES [*e.g., Witek et al*., 2011]. For the dry PBL, this approach has already been applied to Mars by *Colaïtis et al.* [2013]. However, EDMF approaches are amenable to treating both "dry" and "moist" convection, where "dry" refers to the case of free convection resulting purely from heating of the atmospheric column at its base, and "moist" refers to the contribution of heat within the interior of the fluid in upwelling plumes and where the heating rate depends upon the vigor of that upwelling [*e.g., Han and Bretherton*, 2019]. Moist convection is the process behind convective cloud formation, with the additional heating resulting from latent heating as atmospheric gases condense—on Earth this is water vapor, but it can also be methane (on Titan and the gas giant planets) and carbon dioxide (in the Martian atmosphere), *etc*.

However, the DII effect presented in this paper demonstrates an additional form of interior heating that unlike moist convection is not due to latent heating, it instead being due to visible radiative heating of suspended dust. In order to capture the combined effect of "dry" and "dusty" forcing upon convection, an MF scheme will need to be developed from LES, such as that presented, in this paper to be able to link large-scale forcing variables in order to properly predict the depth and vigor of CBL mixing when dust lifting is ongoing. Similarly, the close and bidirectional relationship between DII and dust lifting suggests

that current separate dust lifting and PBL schemes in Mars GCM and mesoscale models would be improved with a unified model of PBL dynamics, mixing, and surface dust lifting.

6.5 Dust Devil Dust Lifting

While LES is capable of modeling convective vortices and dust devils, the model mesh chosen for the bulk of this project would not capture most of the dust devil spectrum (*e.g.*, from the table of large dust devils in Amazonis measured from high resolution images by *Fisher et al.* [2005], only the very widest—at 459m—could even barely be resolved with our 100m mesh spacing). As such, there is a need to examine dust devil statistics within the context of a LES with radiatively and dynamically interactive dust in the future. However, we can examine what the implications of the inhomogeneous dust in the present CBL simulations using the thermodynamic efficiency theory of *Renno et al*. [1998].

Renno et al. [1998] provided a means of quantifying the level of dust devil activity based on the fact that "the flux of mechanical energy made available by the convective heat engine is equal to the flux of energy mechanically dissipated by friction." The *Renno et al.* [1998] dust devil activity (the energy available for convective vortices, Λ) is found to be:

$$\Lambda = (1 - b)F_s \tag{8}$$

and:

$$b \equiv \frac{P_s^{\kappa+1} - P_{top}^{\kappa+1}}{\left(P_s - P_{top}\right)(\kappa + 1)P_s^{\kappa}} \tag{9}$$

Where F_s is the heat input to the CBL at the base, P_s is the surface pressure, P_{top} is the CBL top pressure, and κ is the ratio of the specific gas constant and the specific heat at constant pressure. F_s is properly taken to be the sum of the sensible heat flux from the surface and

the thermal infrared radiative heat flux between the surface and the lowest portion of the atmosphere (from Fig. 9c and 9d we take this depth to be 1km).

Figure 21 shows the sensible and infrared heating terms (Fig. 21a and 21b, respectively), the parameter (1-b) (Fig. 21c), and the dust devil activity, Λ (Fig. 21d), for the FD cases. These results show the roughly comparable contributions of the sensible and radiative heat flux to the heating of the bottom of the CBL, with the sensible heating peaking slightly later in local time than the radiative heating, and with the former also moving to progressively earlier local times as the optical depth increases. Both the sensible and radiative heating decreases with increasing optical depth, but the sensible heat decreases far more significantly, consistent with the dramatic decrease in CBL convection (*c.f.*, Fig. 2). The (1-b) parameter (Fig. 21c) depends significantly upon the CBL depth, and thus it also decreases with optical depth increase and should be compared with Fig. 2b. Also consistent with the CBL depth, (1-b) attains its greatest value in the late afternoon. As the linear product of (1-b) and the sum of the sensible and radiative heating, the dust devil activity, Λ, peaks in the early afternoon and then falls to near zero by the late afternoon (Fig. 21d). Peak Λ decreases by about a factor of 2 as the dust optical depth increases from 0 to 0.5. Thus, there is a very strong negative feedback between increases in optical depth and Λ in the FD cases. This is reflected in the negative feedback for dust devil dust lifting reported in GCM simulations [*e.g., Newman et al*., 2002; *Basu et al.,* 2004; *Newman and Richardson*, 2015; *Kahre et al*., 2017].

Figure 22 shows the same parameters as Fig. 21, but instead for the VD cases. For these cases, the relative insensitivity of the result to dust optical depth is noticeable, even though the optical depth differences between the cases is large by 1700LT (see Fig. 4). The reasons for the reduced sensitivity of the surface-atmosphere temperature contrast to changing optical depth when dust is inhomogeneous are mentioned in Section 5 (the sensible and

radiative heat fluxes are largely controlled by the surface-atmosphere temperature contrast). The control of the (1-b) parameter by the CBL height is illustrated in Fig. 22c, which shows an opposite trend with increasing dust optical depth compared to the FD cases (Fig. 21c). Specifically (1-b) now increases significantly as the optical depth is increased in the mid- and late afternoon. Indeed, the (1-b) parameter shows a larger sensitivity to changing optical depths than the lower CBL heating (Fig. 22a and 22b), and thus the output suggest a slight positive feedback between increasing optical depth and increasing peak dust devil activity, Λ, for the VD cases (Fig. 22d). If this positive feedback does exist—or even the relative lack of sensitivity of Λ to total dust optical depth compared to the traditional strong negative feedback exhibited in Fig. 21d for the FD cases—this suggests that there might be very significant implications for GCM simulations of the global dust cycle, in which dust devils are thought to play a substantial role in maintaining the background haze of dust and in which the strong negative feedback of optical depth upon dust devil lifting is a feature of existing dust devil lifting parameterization [*Newman et al*., 2002; *Basu et al*., 2004; *Kahre et al*., 2017].

The LES cases shown in Fig. 22 were not optimized to study dust devil activity. The noise apparent in the Figure, especially as regarding the weak positive feedback of dust optical depth upon Λ, could be rectified by generating much more frequent output from the LES cases thereby generating more data points at comparable local times (in this initial paper we had to balance the number of cases run against the volume of output needed for storage and processing). However, it would probably be more useful to undertake specific LES experiments designed to explicitly resolve a much larger fraction of the dust devil spectrum and to test the relationship between the simulated dust devil populations, the Λ diagnostic, and the influence of total optical depth and DII on both. Such LES experiments would need between a factor of 10 and 100 decrease in the grid spacing compared to the VD cases in this study, and thus is deferred to a subsequent study.

6.6 Reasonableness of DII Values Examined

Almost all of the VD cases conducted in this study were designed so as to obtain a range of moderate total optical depths which to compare with the FD cases. These simulations yielded visible optical depths in the range of about 0.3-0.6 over an area of about 14 km were examined (with peaks in plumes up to about 0.8). In terms of the DII, the main ensemble of VD cases yielded a peak value of DII< 0.1. In order to initially probe the effect of larger amounts of dust inhomogeneity, dust lifting was modified in simulations required to generate Fig. 20 such that a maximum value of DII=0.23 at τ=0.3 was simulated. It is thus natural to ask how representative of real dust lifting situations on Mars these cases represent.

There are few observations of opacity within dust storms at resolutions close enough to LES for good comparison, but those that do exist find significant dust inhomogeneities at the low end of the mesoscale (thus at the scales of the whole extent of the LES domains considered in this study). *Määtänen et al.* [2009] observed a local dust storm with OMEGA that appeared to consist of at least "rounded plumes" of dust with τ>6 that were 5-10 km in diameter, and that alternated with areas of much clearer air of similar scale. This yields an equivalent DII>0.5. *Heavens* [2017] describes large local dust storms in the northern mid-latitudes in Mars Orbiter Camera (MOC) and Mars Color Imager (MARCI) [Malin et al., 1992, 2001] images that consist of alternating bands of dustier and clear air of 15-50 km thickness with opacities ranging from 0.4-1.4, implying a DII of ~0.4. On somewhat shorter length scales, the dust lifting plumes capture in THEMIS visible images and shown by *Inada et al*. [2007] yield sharp optical depth variations on scales as a short as 650m. While the optical depths were not retrieved from these images, the dust clouds obscure the surface below the convective roll plumes, suggesting DII values at least as large at the OMEGA, MOC, and MARCI images. The THEMIS images also suggest that the primary

mechanism causing dust inhomogeneity—namely concentration of dust into upwelling plumes and sheets—is actually at play in the real atmosphere. An example of the structure of dust lifted in convective rolls from THEMIS imagery is shown in Figure 23a.

The very much higher values of DII implied by the observations and for large values of optical depth suggest that the strength of positive dust feedback on the augmentation of CBL turbulence and the lifting of dust may be underestimated in this study, although it is possible that at very large dust optical depths the shadowing of the surface—or indeed, the self-shadowing of much of the thermals—may come to dominate over the augmenting differential heating. This is an interesting question that requires further study in more extreme dust injection rate LES cases designed to simulate very small-scale dust storms and dust lifting plumes, such as those shown in Fig. 23a. However, the observations also suggest that the simulations and the DII values reported in this paper are not probably excessive for moderate dust lifting, such as might be associated with modest dust devil activity and/or putative wind gust dust lifting that does not lead to distinct local storms identifiable in imagery.

6.7 The Dust Opacity / Dust Lifting Feedback on Larger Scales

This study has examined dust lifting and dust concentration in isolation at the microscale (*i.e.*, on scales equal to and shorter than that of the largest CBL convection cells). However, spacecraft imagery provides ample evidence of various types of "textures" on the topside of dust storms at scales that extend continuously from hundreds of meters to hundreds of kilometers (Fig. 23). Texture elements within dust storms are common in MOC and MARCI wide-angle camera images (a few km/pix) and are also corroborated by opportunistic narrow-angle camera images (down to a few m/pix) [*Inada et al*., 2007; *Määtänen et al.,* 2009; *Guzewich et al*., 2017; *Kulowski et al*., 2017; *Toigo et al*., 2018].

These observed textures at micro- and mesoscales are potentially indicative of the dynamics operating within dust storms from the very smallest of scales. The LES examined in this work suggest that even at relatively low optical depths and relatively modest DII, positive feedback exists between optical depth and vertical dust mixing and potentially dust lifting from the surface. Ultimately, larger scale storm systems are initially composed of individual PBL plumes, cells, and rolls, as visually exemplified in Fig. 23a, where the growth from small scale plumes to larger consolidated dust clouds can be seen from image right to image left (which is almost certainly the downstream wind direction). Thus, an important question for future work is how the microscale feedbacks demonstrated here might influence the mesoscale and larger dust clouds observed in the atmosphere. Are such feedbacks important at the tops and/or at the periphery of local storm systems and are they involved in storm growth? And to what degree are the microscale mechanisms of storm growth responsible for the growth of dust up to the extent where distinct mesoscale modes of growth become important? Are there mechanisms of storm expansion that involve individual dusty cells / plumes causing the excitation of neighboring cells through the lateral leakage of momentum and/or dust? The existence of some feedback at microscales demonstrated in this paper suggests that further LES experiments with larger domains that cross the micro/mesoscale boundary are warranted.

7. Summary

In this work we employed a validated version of the MarsWRF in LES mode to examine the differences in convective boundary layer (CBL) dynamics between: 1) idealized uniform distributions of radiatively active dust (the fixed dust or FD cases in this paper) and 2) more realistic dust distributions that would occur when dust lifting is ongoing in which the dust is self-consistently concentrated into upwelling plumes (the variable dust or VD cases in this paper). The FD cases are also likely to be valid in cases where no active

dust lifting is occurring, and the dust distribution has been largely homogenized by CBL mixing over several prior sols.

The CBL behavior for the FD cases was found to agree with expectations based upon the effect of atmospheric dust in shading the surface. With increasing optical depth, the surface-atmosphere temperature decreases and hence the heat flux (which both sensible and radiative) from the surface into the lower portion of the CBL also decreases. This causes a decrease in the energy injected into the CBL (a reduction in the TKE), a reduction in both the Deardorff (convection) velocity scale and maximum vertical plume speeds, a reduction of the surface layer wind stresses associated with the turbulent motions, and a reduction in the depth of the CBL. This influence of dust optical depth upon the CBL dynamics has previously been widely noted, and if it represented the whole story as applied to dust lifting would produce a negative feedback [*e.g.*, *Newman et al*., 2002; *Kahre et al*., 2006]. Specifically, increased dust optical depth would decrease CBL wind stresses (reducing lifting due to gusts in the CBL) and would also decrease the thermodynamic efficiency of the convective vortices that form dust devils [*Renno et al*., 1998]. In both cases, dust lifting potential would decrease as the optical depth increases, and the depth of the dust lifting would become shallower as dust optical depth increases.

With fully interactive dust (the VD cases) the CBL exhibits quite difference behavior relative to the FD cases. Comparing FD and VD cases at similar total optical depths in the mid-afternoon, the differences in the dust distribution are twofold: 1) there are significant lateral differences in dust optical depth, which can be characterized with a Dust Inhomogeneity Index, $DII=\sigma_\tau/\tau_{avg}$ (see also Eqn. 10), where σ_τ is the lateral standard variation of the dust opacity and τ_{avg} is the lateral average, and 2) there are differences in the vertical dust distribution where the process of active dust lifting tends to have more of the dust near the surface in the VD cases versus FD cases for the same total optical depth.

Both aspects of the dust distribution tend to influence the CBL dynamics when comparing FD and VD cases. Specifically, for the same mid-afternoon optical depth, the VD cases exhibit larger surface/atmosphere temperature contrasts, larger heat fluxes into the CBL, larger TKE in the CBL, larger Deardorff and updraft plume speeds, larger near-surface wind stresses, and deeper CBL. The mechanisms of augmentation of the VD cases are found to be threefold: 1) the laterally inhomogeneous dust distribution causes visible radiative heating to be preferentially concentrated within the upwelling plumes, injecting additional buoyancy and hence TKE directly into CBL convection, 2) relatively smaller total dust optical depth within CBL downwelling regions allows higher surface temperatures, higher surface/atmosphere temperature contrasts, and hence greater surface/atmosphere exchange of heat, and 3) the relatively clearer atmosphere above the CBL top in the VD versus the FD cases means slightly cooler free atmospheric temperatures and hence greater ease of vertical penetration of the CBL as it grows.

The impact of dust lifting rates on the DII and on the CBL dynamics were also examined within the VD ensemble of runs. As the lifting rate—and hence afternoon optical depths—increase, the surface temperature does decrease, but does to a much lesser degree than for comparable changes of opacity between FD runs. This reduced efficacy of shading appears to be due to the concentration of the dust optical depth into the plumes, leaving relatively clear air over much of the surface. With the surface-atmosphere temperature contrast response to increased domain-average opacity very much muted compared to similar changes within the FD ensemble, the surface/atmosphere heat flux is little changed and hence the expected CBL vigor, in terms of the modified Deardorff vertical velocity is also muted. Indeed, until the later afternoon, the Deardorff vertical velocity, the vertical maximum plume speeds, the surface frictional velocities, and the TKE per unit mass of air are insensitive to the optical depth, such that there appears to be no negative feedback of optical depth on the CBL vigor. However, there is a notable increase in the CBL depth with

the rate of dust injection / total optical depth. If one were to use the *Renno et al.* [1998] heat engine scaling to assess the activity of dust devil dust lifting [*e.g., Newman et al.*, 2002], the insensitivity of the surface/atmosphere heat flux to increased optical depth and the significant positive feedback of CBL depth with optical depth would suggests that there will be in fact be a positive feedback for dust devil lifting when the dust is not uniformly distributed. The increased CBL height also suggests that even for moderate lifting rates and moderate DII values, dust is lifted several kilometers deeper into the atmosphere than predicted based upon models using uniform dust.

Appendix A. The Sub Grid Scale / Sub Filter Scale Parameterization

A significant difference between the microscale LES and the meso- and synoptic-scale application of MarsWRF is in the treatment of sub grid scale (SGS) mixing and dissipation. In meso-/synoptic-scale application, the SGS parameterization provides a representation of the mixing of heat, momentum, and tracers due to all microscale motions (*i.e.*, the full spectrum of PBL eddies) from the largest Bénard cell down to dissipation length scales. The numerical mesh for meso/synoptic scale modeling is always at least an order of magnitude more tightly spaced vertically than it is horizontally (*i.e.*, $\Delta x > 10\Delta z$). The reason for this is that atmospheric motions are approximately hydrostatic at synoptic- and the larger mesoscales, with the characteristic horizontal wavelength being much longer than the vertical wavelength. Thus, for synoptic and hydrostatic mesoscale models, a simple local model of diffusion in the horizontal is always paired with a more complex model of vertical PBL mixing that often involves nonlocal contributions. For nonhydrostatic motions that are much more important at the microscales of the CBL, the horizontal scale becomes comparable with vertical scale. Thus, for LES the model mesh is more similarly spaced in the horizontal and the vertical, and unresolved mixing and dissipation is treated

with 3D parameterization. Since the dominant PBL eddies are resolved by design in LES, the PBL parameterization is deactivated.

The reason that any SGS parameterization is needed in LES is that while LES captures most of the microscale dynamical length scales, it is not Direct Numerical Simulation (DNS) and thus does not capture the motions all the way down to the length scales of dissipation (*i.e.*, the Kolmogorov length scale) at about 0.1-10 mm [*e.g.*, *Stull*, 1988]. In practice, for reasons of computational efficiency, LES is generally implemented with a mesh spacing of roughly 1-100 m. As such, LES still requires SGS parameterization of eddy diffusion for scales between the grid scale and the dissipation scale (it should be noted that the term sub filter scale (SFS) parameterization is often more accurately used instead of SGS since representation of motions on scales below those *fully resolved* by the model is actually what is required, and that the effective numerical filter scale of the mesh is always larger than the grid scale due to numerical discretization error.)

WRF contains several different SGS/SFS parameterizations, with some significantly more complex than others. The two least complex and most widely used SGS/SFS parameterizations available within WRF are three-dimensional local eddy diffusivity models in which the diffusivity/viscosity is calculated from either 1) the resolved wind field deformation and static stability (in the "Smagorinsky scheme"), or 2) the prognostic SGS/SFS turbulence kinetic energy (TKE, in the "SGS/SFS TKE scheme"). In this study, we specifically use the SGS/SFS TKE scheme.

In this appendix, we describe the relationship between the calculation of diffusivity/viscosity in the Smagorinsky and SGS/SFS TKE schemes [*Lilly* 1966; *Moeng* 1984]. We also provide a formulation for diagnosing the subgrid scale TKE from the Smagorinsky scheme.

A.1 Relationship Between Diffusivity/Viscosity and TKE Within the Smagorinsky and TKE SGS/SFS Parameterizations

For understanding the evolution of the PBL (and for many approaches to parameterizing PBL mixing) an understanding of the total budget of TKE is required. In LES, the total PBL TKE must be constructed as the sum of the resolved-scale TKE and the SGS/SFS parameterized TKE. In the case of the widely used "3D Smagorinsky" scheme [*Smagorinsky*, 1963], and unlike the SGS/SFS TKE scheme, the TKE on unresolved scales is not prognostic and must be diagnosed from the model. In the remainder of this section, we provide a discussion of what processes influence the SGS/SFS TKE budget and how the subgrid scale TKE, the 3D flow deformation, and the static stability are related; and how each relates to the viscosity/diffusivity.

The formulation of both the Smagorinsky and TKE SGS/SFS schemes is based on the assumption that subgrid scale eddies act analogously to molecular viscosity [*Lilly*, 1966]. As such, subgrid-scale stresses can be treated as a viscous response to the deformation of the model-resolved motion. The deformation is given by the strain rate tensor calculated from the model-resolved winds [*Lilly* 1966, *Moeng* 1984]:

$$S_{ij} = \frac{1}{2}\left(\frac{\partial u_i}{\partial x_j} + \frac{\partial u_j}{\partial x_i}\right) \tag{A1}$$

where the indices *i*,*j* refer to orthogonal coordinate directions and may have values 1, 2, or 3, with the distance in each of these directions given by x_i, and the components of the resolved wind field in each of these directions by u_i. The strain rate itself can be visualized as being composed of two parts, a component of net radial expansion or compression of

the flow, and a component of volume conservative shearing of the flow. The subgrid-scale stresses, which build up within the fluid as a result of this resolved strain and act to oppose the strain, depend on the eddy viscosity of the fluid. Within a completely inviscid fluid, no stress would develop at all. In general, the eddy viscous stress (or more accurately, the stress per unit fluid density) is given by:

$$\tau_{ij} = -2\nu S_{ij} \tag{A2}$$

where τ_{ij} is the stress acting upon the resolved flow due to the subgrid scale eddies, and ν is the kinematic eddy viscosity. Once calculated, the stresses are used within the model to calculate resolved wind field tendencies:

$$\left(\frac{\partial u_i}{\partial t}\right)_{eddy\ visc} = -\sum_j \frac{\partial \tau_{ij}}{\partial x_j} \tag{A3}$$

The two schemes differ in their estimate of eddy viscosity. The 3D Smagorinsky scheme [*Smagorinsky*, 1963; *Lilly*, 1966] determines the viscosity from the strain rate tensor and from the static stability:

$$\nu_{smag} = (c_s l)^2 \left(\sqrt{\left(\sum_{i,j} S_{ij} S_{ij} \right) - \frac{N^2}{P_r}} \right) \tag{A4}$$

where c_s is a constant (taken to be 0.25), l is a length scale set by the model grid spacing, with $l=(\Delta x_i \Delta x_j \Delta x_k)^{1/3}$, N is the Brunt–Väisälä frequency:

$$N = \sqrt{\frac{g}{\theta}\frac{\partial \theta}{\partial z}} \tag{A5}$$

with g being the acceleration due to gravity, θ being the potential temperature, and z being the vertical distance ($z=x_k$ by convention) and P_r is the turbulent Prandtl number—the

unitless ratio of the momentum diffusivity (*i.e.*, the viscosity, ν) and the thermal diffusivity, α, $P_r \equiv \nu/\alpha$, which is taken to have a constant value of 1/3 (*i.e.*, once the viscosity, ν, is calculated for either the Smagorinsky or SGS/SFS TKE scheme, the diffusivity is then simply the viscosity divided by the Prandtl number). The square root in Eqn. A4 is only taken when the value would not result in an imaginary number, otherwise it is set to zero. In order to maintain computational stability, a lower limit of 10^{-6} m^2/s is imposed for ν_{smag} when modeling the atmospheres of Earth and Mars.

The formulation of Eqn. A4 suggests that the eddy viscosity has two sources. The first source is the mechanical generation of turbulence due to the resolved fluid deformation and captured by the first term in the square toot in Eqn. A4. The second source corresponds to the thermal generation of turbulence and is due to buoyancy, which we identify as $-N^2$ in Eqn. A4. Note that the buoyancy can be negative (*i.e.*, if the Brunt–Väisälä frequency is a real number and hence N^2 is positive), in this case the static stability of the air tends to damp turbulence. In the limit of strong static stability (strongly negative buoyancy), ν_{smag} is limited to its minimum value given in the prior paragraph.

The SGS/SFS TKE scheme is similar in its closure approach to 1.5 order (also known as 2.5 *level* closure) TKE PBL schemes used in meso- and synoptic scale modeling, except that diffusion is applied in all three spatial dimensions in the SGS/SFS scheme. The TKE SGS/SFS scheme carries a prognostic subgrid scale TKE (*i.e.*, the value of the unresolved component of the total TKE) but the scheme does not prognose any other 2nd order subgrid variables (the subgrid TKE is second order as it is the product of the subgrid scale wind perturbations with themselves, *i.e.* $\Sigma u_i' u_i'$ for i=1,2,3). The viscosity is estimated from the subgrid scale TKE as [*Lilly*, 1966; *Klemp and Wilhelmson*, 1978]:

$$\nu_{tke} = c_e l \left(\sqrt{(TKE_{SGS})} \right)$$

(A6)

where c_e is a constant taken to be 0.15. The TKE_{SGS} is prognosed by calculation of TKE_{SGS} generation due to buoyancy and flow deformation, through local vertical and horizontal diffusion, and dissipative loss to heat. The TKE_{SGS} is advected by the resolved three-dimensional wind field. The TKE_{SGS} tendency is calculated as [*Klemp and Wilhelmson*, 1978]:

$$\frac{\partial(TKE_{SGS})}{\partial t} = \left[-\nu_{tke}N^2 + \frac{g}{\theta}\frac{(HFX)}{\rho c_p}\right] + \left[\nu_{tke}\left(\sum_{i,j} S_{ij}S_{ij}\right) - \frac{u_*^2}{U}\left(\sum_{i=1}^{2} u_i S_{i3}\right)\right] + \left[\sum_{i=1}^{3}\frac{\partial}{\partial x_i}\left(\nu_{tke}\frac{\partial(TKE_{SGS})}{\partial x_i}\right)\right] - \frac{c_e}{l}(TKE_{SGS})^{\frac{3}{2}}$$

(A7)

where HFX is the heat flux from the surface into the atmosphere, which is either prescribed or calculated from the model surface layer parameterization (HFX is a two dimensional field representing the flux at the bottom boundary of the atmosphere), ρ is the air density, c_p is the atmospheric specific heat capacity at constant pressure, u_* is the frictional or drag velocity, which is either prescribed or calculated from the surface layer parameterization (like HFX, u_* is zero in all but the lowest model layer), and U is the magnitude of the total resolved horizontal wind speed. The surface layer scheme used in the microscale/LES simulations in this paper is the same one used when the MarsWRF mesoscale or global model is run (*i.e.*, the MRF/YSU PBL scheme [*Hong et al.*, 2006; *Toigo et al.*, 2012]). For LES, we only use the surface layer component [*Jimenez et al*., 2012], with the rest of the PBL scheme inactive.

Diffusion of tracers is assumed to operate with the same diffusivity as heat. TKE_{SGS} is a useful metric of the subgrid scale turbulence and although it is not explicitly used in the 3D Smagorinsky scheme, it can be inferred for the 3D Smagorinsky scheme from the

viscosity, and hence from the deformation and static stability due to the equivalency of Eqn. A3 and A5 (note again that this is the inferred SGS/SFS TKE):

$$TKE_{infer} = \left(\frac{\nu_{smag}}{c_e l}\right)^2 = \left(\frac{c_s^2 l}{c_e}\right)^2 \left[\left(\sum_{i,j} S_{ij} S_{ij}\right) - \frac{N^2}{P_r}\right] \quad \text{(A8)}$$

Acknowledgments

ZW, TL, and JC would like to acknowledge supports from the B-type Strategic Priority Program of the Chinese Academy of Sciences, Grant XDB41000000 and the National Natural Science Foundation of China through grants 41525015, 41774186, 42004147, and 41674149. MIR, NGH, CEN and MLW would like to acknowledge support from NASA grant NNX15AI33G to Hampton University. XZ acknowledges support from NSF grant AST1740921. Resources supporting this work were provided by the NASA High-End Computing (HEC) Program through the NASA Advanced Supercomputing (NAS) Division at Ames Research Center. The MarsWRF model output used in this study has been archived on data.mendeley.com (http://dx.doi.org/10.17632/4m96z77k4c.1)

References

Basu, S., Richardson, M. I., & Wilson, R. J. (2004). Simulation of the Martian dust cycle with the GFDL Mars GCM. Journal of Geophysical Research: Planets, 109(E11).

Cantor, B. A., James, P. B., Caplinger, M., & Wolff, M. J. (2001). Martian dust storms: 1999 Mars orbiter camera observations. Journal of Geophysical Research: Planets, 106(E10), 23653-23687.

Colaïtis, A., A. Spiga, F. Hourdin, C. Rio, F. Forget, and E. Millour (2013), A thermal plume model for the Martian convective boundary layer, *J. Geophys. Res.*, *118*(7), 1468-1487, doi:10.1002/jgre.20104.

Conrath, B. J. (1975), Thermal Structure Of Martian Atmosphere during Dissipation Of Dust Storm Of 1971, *Icarus*, *24*(1), 36-46, doi:Doi 10.1016/0019-1035(75)90156-6.

Couvreux, F., F. Hourdin, and C. Rio (2009), Resolved Versus Parametrized Boundary-Layer Plumes. Part I: A Parametrization-Oriented Conditional Sampling in Large-Eddy Simulations, *Boundary-Layer Meteorology*, *134*(3), 441-458, doi:10.1007/s10546-009-9456-5.

Daerden, F., Whiteway, J. A., Neary, L., Komguem, L., Lemmon, M. T., Heavens, N. G., Cantor, B. A., Hébrard, E., and Smith, M. D. (2015), A solar escalator on Mars: Self-lifting of dust layers by radiative heating, Geophys. Res. Lett., 42, 7319– 7326, doi:10.1002/2015GL064892.

Fisher, J.A., Richardson, M.I., Newman, C.E., Szwast, M.A., Graf, C., Basu, S., Ewald, S.P., Toigo, A.D.,Wilson, R.J., 2005. A survey of martian dust devil activity usingmars global surveyor mars orbiter camera images. *J. Geophys. Res*. 110, doi:10.1029/2003JE002165.

Fuerstenau, S. D. (2006), Solar heating of suspended particles and the dynamics of Martian dust devils, Geophys. Res. Lett., 33, L19S03, doi:10.1029/2006GL026798.

Gierasch, P. And R. Goody (1968), A study of the thermal and dynamical structure of the martian lower atmosphere. Planet. Space Set. 1968. Vol. 16., 615-646.

Goody, R., and M. J. S. Belton (1967), A discussion of Martian atmospheric dynamics, *Planetary and Space Science*, *15*(2), 247-256, doi:https://doi.org/10.1016/0032-0633(67)90193-6.

Guzewich, S.D., A.D. Toigo, L. Kulowski, H. Wang (2015). Mars Orbiter Camera climatology of textured dust storms. Icarus. 258:1-13, doi: 10.1016/j.icarus.2015.06.023

Guzewich, S. D., Toigo, A. D. and Wang, H., An investigation of dust storms observed with the Mars Color Imager, Icarus, 289, 199-213, doi:10.1016/j.icarus.2017.02.020, 2017.

Han, J., & Bretherton, C. S. (2019). TKE-based moist Eddy-Diffusivity Mass-Flux (EDMF) parameterization for vertical turbulent mixing. Weather and Forecasting, 34(4), 869-886.

Heavens, N. G. (2017). Textured dust storm activity in northeast Amazonis–southwest Arcadia, Mars: Phenomenology and dynamical interpretation. Journal of the Atmospheric Sciences, 74(4), 1011-1037.

Heavens, N. G., M. I. Richardson, A. Kleinböhl, D. M. Kass, D. J. McCleese, W. Abdou, J. L. Benson, J. T. Schofield, J. H. Shirley, and P. M. Wolkenberg (2011), The vertical distribution of dust in the Martian atmosphere during northern spring and summer: Observations by the Mars Climate Sounder and analysis of zonal average vertical dust profiles, J. Geophys. Res., 116(E4), doi:10.1029/2010je003691.

Hinson, D. P., M. Pätzold, S. Tellmann, B. Häusler, and G. L. Tyler (2008), The depth of the convective boundary layer on Mars, *Icarus*, *198*(1), 57-66, doi:10.1016/j.icarus.2008.07.003.

Hong, S.-Y., Y. Noh, and J. Dudhia (2006), A New Vertical Diffusion Package with an Explicit Treatment of Entrainment Processes, *Monthly Weather Review*, *134*(9), 2318-2341, doi:10.1175/mwr3199.1.

Inada, A., M.I. Richardsona, T.H. McConnochie, M.J. Strausberg, H. Wang d, J.F. Bell III (2007). High-resolution atmospheric observations by the Mars Odyssey Thermal Emission Imaging System. Icarus 192 (2007) 378–395, doi:10.1016/j.icarus.2007.07.020

Jiménez, P. A., Dudhia, J., González-Rouco, J. F., Navarro, J., Montávez, J. P., & García-Bustamante, E. (2012). A revised scheme for the WRF surface layer formulation. Monthly Weather Review, 140(3), 898-918.

Kahre, M. A., Murphy, J. R., & Haberle, R. M. (2006). Modeling the Martian dust cycle and surface dust reservoirs with the NASA Ames general circulation model. Journal of Geophysical Research: Planets, 111(E6).

Kahre, M. A., Murphy, J. R., Newman, C. E., Wilson, R. J., Cantor, B. A., Lemmon, M. T., & Wolff, M. J. (2017). The Mars dust cycle. The atmosphere and climate of Mars, 18, 295.

Klemp, J. B., and R. B. Wilhelmson (1978), The Simulation of Three-Dimensional Convective Storm Dynamics, *J. Atmos. Sci.*, *35*(6), 1070-1096, doi:10.1175/1520-0469(1978)035<1070:tsotdc>2.0.co;2.

Kulowski, L., H. Wang, A.D. Toigo, The seasonal and spatial distribution of textured dust storms observed by Mars Global Surveyor Mars Orbiter Camera. Adv. Space Res., 59, 715-721, doi:10.1016/j.asr.2016.10.028, 2017.

Lee, C., Lawson, W. G., Richardson, M. I., Anderson, J. L., Collins, N., Hoar, T., & Mischna, M. (2011). Demonstration of ensemble data assimilation for Mars using DART, MarsWRF, and radiance observations from MGS TES. Journal of Geophysical Research: Planets, 116(E11).

Lee, C., M. I. Richardson, C. E. Newman, and M. A. Mischna (2018), The sensitivity of solsticial pauses to atmospheric ice and dust in the MarsWRF General Circulation Model, Icarus, 311, 23-34.

Lilly, K. (1966), The representation of small-scale turbulence in numerical simulation experiments.

Määttänen, A., Fouchet, T., Forni, O., Forget, F., Savijärvi, H., Gondet, B., Melchiorri, R., Langevin, Y., Formisano, V., Giuranna, M. Bibring, J. P. (2009). A study of the properties of a local dust storm with Mars Express OMEGA and PFS data. Icarus, 201(2), 504-516.

Martinez, G. M., C. N. Newman, A. De Vicenteretortillo, E. Fischer, N. O. Renno, M. I. Richardson, A. G. Fairen, M. Genzer, S. D. Guzewich, and R. M. Haberle (2017), The Modern Near-Surface Martian Climate: A Review of In-situ Meteorological Data from Viking to Curiosity, Space Science Reviews, 212(1), 295-338.

Michaels, T. I., and S. C. Rafkin (2004), Large ‐ eddy simulation of atmospheric convection on Mars, Quarterly Journal of the Royal Meteorological Society, 130(599), 1251-1274.

Mischna, M. A., C. Lee, and M. Richardson (2012), Development of a fast, accurate radiative transfer model for the Martian atmosphere, past and present, J. Geophys. Res., 117(E10), doi:10.1029/2012je004110.

Moeng, C.-H. (1984). A Large-Eddy-Simulation Model for the Study of Planetary Boundary- Layer Turbulenc. Journal of Atmospheric Sciences, 41(13):2051–2062.

Moeng, C.-H., and J. C. Wyngaard (1989): Evaluation of turbulent transport and dissipation closures in second-order modeling. J. Atmos. Sci., 46, 2311-2330.

Moeng, C. H., & Sullivan, P. P. (1994). A comparison of shear-and buoyancy-driven planetary boundary layer flows. Journal of the Atmospheric Sciences, 51(7), 999-1022.

Montmessin, F., Forget, F., Rannou, P., Cabane, M., & Haberle, R. M. (2004). Origin and role of water ice clouds in the Martian water cycle as inferred from a general circulation model. Journal of Geophysical Research: Planets, 109(E10).

Neakrase, L. D., Greeley, R., Iversen, J. D., Balme, M. R., & Eddlemon, E. E. (2006). Dust flux within dust devils: Preliminary laboratory simulations. Geophysical research letters, 33(19).

Newman, C. E., & Richardson, M. I. (2015). The impact of surface dust source exhaustion on the martian dust cycle, dust storms and interannual variability, as simulated by the MarsWRF General Circulation Model. Icarus, 257, 47-87.

Newman, C. E., S. R. Lewis, P. L. Read, and F. Forget (2002), Modeling the Martian dust cycle, 1. Representations of dust transport processes, *J. Geophys. Res.*, *107*(E12), 6-1-6-18, doi:10.1029/2002je001910.

Newman, C. E., J. Gómez-Elvira, M. Marin, S. Navarro, J. Torres, M. I. Richardson, J. M. Battalio, S. D. Guzewich, R. Sullivan, M. d. l. Torre, A. R. Vasavada, and N. T. Bridges (2017), Winds measured by the Rover Environmental Monitoring Station (REMS) during the Mars Science Laboratory (MSL) rover's Bagnold Dunes Campaign and comparison with numerical modeling using MarsWRF, *Icarus*, *291*, 203-231, doi:https://doi.org/10.1016/j.icarus.2016.12.016.

Petrosyan, A., et al. (2011), The Martian atmospheric boundary layer, Rev. Geophys., 49, RG3005, doi:10.1029/2010RG000351

Powers, J. G., et al. (2017), The Weather Research and Forecasting Model: Overview, System Efforts, and Future Directions, *Bulletin of the American Meteorological Society*, *98*(8), 1717-1737, doi:10.1175/bams-d-15-00308.1.

Rafkin, S. C. R., J. L. Hollingsworth, M. A. Mischna, C. E. Newman, and M. I. Richardson (2013), Mars: Atmosphere and climate overview, *Comparative Climatology of Terrestrial Planets*, *1*, 55-89.

Renno, N. O., Burkett, M. L., & Larkin, M. P. (1998). A simple thermodynamical theory for dust devils. Journal of the atmospheric sciences, 55(21), 3244-3252.

Richardson, M. I., and Newman, C. E. (2018). On the relationship between surface pressure, terrain elevation, and air temperature. Part I: The large diurnal surface pressure range at Gale Crater, Mars and its origin due to lateral hydrostatic adjustment. Planetary and Space Science, 164, 132-157.

Richardson, M. I., W. R. John, and A. V. Rodin (2002), *Water ice clouds in the Martian atmosphere: General circulation model experiments with a simple cloud scheme*, 2-1–2-29 pp.

Richardson, M. I., A. D. Toigo, and C. E. Newman (2007), PlanetWRF: A general purpose, local to global numerical model for planetary atmospheric and climate dynamics, *J. Geophys. Res.*, *112*(E9), doi:10.1029/2006je002825.

Savijarvi, H. (1999), A model study of the atmospheric boundary layer in the Mars pathfinder lander conditions, Quarterly Journal of the Royal Meteorological Society, 125(554), 483-493.

Savijärvi, H., A. Määttänen, J. Kauhanen, and A.-M. Harri (2004), Mars Pathfinder: New data and new model simulations, *Quarterly Journal of the Royal Meteorological Society*, *130*(597), 669-683, doi:10.1256/qj.03.59.

Siebesma, A. P., and J. Teixeira, 2000: An advection-diffusion scheme for the convective boundary layer: Description and 1d-results. *14th Symp. on Boundary Layers and Turbulence*, Aspen, CO, Amer. Meteor. Soc., 4.16, https://ams.confex.com/ams/AugAspen/techprogram/paper_14840.htm.

Siebesma, A. P., P. M. M. Soares, and J. Teixeira, 2007: A combined eddy-diffusivity mass-flux approach for the convective boundary layer. J. Atmos. Sci., 64, 1230–1248, https://doi.org/10.1175/JAS3888.1.

Smagorinsky, J. (1963), General Circulation Experiments With The Primitive Equations, *Monthly Weather Review*, *91*(3), 99-164, doi: 10.1175/1520-0493(1963)091<0099:GCEWTP>2.3.CO;2.

Spiga, A. The Planetary Boundary Layer of Mars, Oxford Research Encyclopedia, Planetary Science, doi: 10.1093/acrefore/9780190647926.013.130

Spiga, A., F. Forget, S. R. Lewis, and D. P. Hinson (2010), Structure and dynamics of the convective boundary layer on Mars as inferred from large-eddy simulations and remote-sensing measurements, *Quarterly Journal of the Royal Meteorological Society*, n/a-n/a, doi:10.1002/qj.563.

Spiga, A., D. P. Hinson, J.-B. Madeleine, T. Navarro, E. Millour, F. Forget, and F. Montmessin (2017), Snow precipitation on Mars driven by cloud-induced night-time convection, *Nature Geoscience*, *10*(9), 652-657, doi:10.1038/ngeo3008.

Stull, R. B. (1988), *An introduction to boundary layer meteorology*, Kluwer Acad., Norwell, Mass.

Temel, O., C.B. Senel, S. Porchetta, D. Munoz-Esparza, M.A. Mischna, T. Van Hoolst, J. van Beeck and O. Karatekin (2020), Large eddy simulations of the Martian convective boundary layer: Towards developing a new planetary boundary layer scheme, Atmospheric Research.

Toigo, Anthony D., Mark I. Richardson, Huiqun Wang, Scott D. Guzewich, and Claire E. Newman. "The cascade from local to global dust storms on Mars: Temporal and spatial thresholds on thermal and dynamical feedback." Icarus 302 (2018): 514-536.

Toigo, A. D., C. Lee, C. E. Newman, and M. I. Richardson (2012), The impact of resolution on the dynamics of the martian global atmosphere: Varying resolution studies with the MarsWRF GCM, *Icarus*, *221*(1), 276-288, doi:10.1016/j.icarus.2012.07.020.

Toigo, A. D., M. I. Richardson, S. P. Ewald, and P. J. Gierasch (2003), Numerical simulation of Martian dust devils, *J. Geophys. Res.*, *108*(E6), doi:Artn 5047 10.1029/2002je002002.

Witek, M. L., Teixeira, J., & Matheou, G. (2011). An integrated TKE-based eddy diffusivity/mass flux boundary layer closure for the dry convective boundary layer. Journal of the atmospheric sciences, 68(7), 1526-1540.

Wolff, M. J., & Clancy, R. T. (2003). Constraints on the size of Martian aerosols from Thermal Emission Spectrometer observations. Journal of Geophysical Research: Planets, 108(E9).

Table 1. Four LES simulations (cases a, b, c and i in *Hinson* et al. [2008]) carried out for comparison with *Spiga et al*. [2010]

	L_s (°)	Lat (°N)	Long (°E)	Thc (tiu)	Albedo	Znt （m）	$T_{s,max}$ (K)	θ_{mix} (K)	P_s (Pa)
a	**47.1**	**21.8**	**205.0**	**55**	**0.27**	**0.01**	**278**	**221**	**868**
b	**51.2**	**13.7**	**204.6**	**50**	**0.30**	**0.01**	**275**	**220**	**854**
c	**52.1**	**12.3**	**237.2**	**60**	**0.30**	**0.01**	**275**	**250**	**482**
i	**47.8**	**20.6**	**74.0**	**300**	**0.13**	**0.01**	**270**	**233**	**630**

L_s is the areocentric long*itude*, **Lat** *is the north latitude*, **Long** *is the east longitude*, **Thc** *is the thermal inertia (1 tiu= 1 J* m^{-2} K^{-1} $s^{-1/2}$*)*, **Znt** *is the surface roughness,* **$T_{s,max}$** *is the maximum surface temperature in the daytime (between roughly 12 to 13 pm),* **θ_{mix}** *is the potential temperature in the mixed layer at 5 pm and* **P_s** *is the surface pressure.*

Table 2. CBL depths in kilometers predicted by MarsWRF, estimated from radio science occultation retrievals by *Hinson* et al. [2008]), and predicted by the LMD-LES by *Spiga et al*. [2010] for the profile cases a, b, c and i as defined by *Hinson* et al. [2008].

Case	MarsWRF	Observations	LMD-LES
a	**6.1 (19.6%)**	**5.1**	**5.9 (15.7%)**
b	**5.7 (35.7%)**	**4.2**	**5.3 (26.2%)**
c	**7.9 (-3.66%)**	**8.2**	**7.8 (-4.88%)**
i	**7.3 (-27%)**	**10**	**7.4 (-26%)**

The error of the MarsWRF and LMD-LES estimates compared to the observations is shown as a percentage of the observationally inferred CBL depth in parenthesis for both models, i.e., error = (model-observation) / observation.

Table 3. Sensitivity of the modelled Martian boundary layer depth z_i (average value between 1700 and 1730 LT) to the LES resolution, domain size, and model top.

Mesh Name	Grid $N_x \times N_y \times N_z$	dx (m)	dz_1 (m)	dz_t (m)	x (km)	z (km)	z_i (km)
1	**290×290×100**	**50**	**8**	**242**	**14.5**	**12**	**7.29**
2	**145×145×100**	**100**	**8**	**242**	**14.5**	**12**	**7.23**
3*	**145×145×100**	**100**	**10**	**247**	**14.5**	**15**	**7.27**
4	**50×50×75**	**100**	**25**	**260**	**5**	**15**	**6.91**
5	**125×125×75**	**100**	**25**	**268**	**12.5**	**15**	**7.18**
6	**50×50×50**	**100**	**66**	**327**	**5**	**15**	**6.72**
7	**200×200×100**	**100**	**10**	**247**	**20**	**15**	**7.31**

Nx, Ny, and Nz are the number of grid points in the mesh in the two horizontal (x and y) and vertical (z) directions.

dx is the horizontal grid spacing (which always equals dy in all LES presented in this paper).

dz_1 is the model layer thickness at the base of the column (i.e., the layer closest to the surface).

zi, is the predicted height of the top of the CBL at the forecast time (1700-1730 LT).

dzt is model layer thickness at zi.

x is the total domain extent in both the x and y (horizontal) directions.

z is the total domain extent in the vertical.

** indicates that mesh 3 is the selected default mesh used in most experiments described in this paper.*

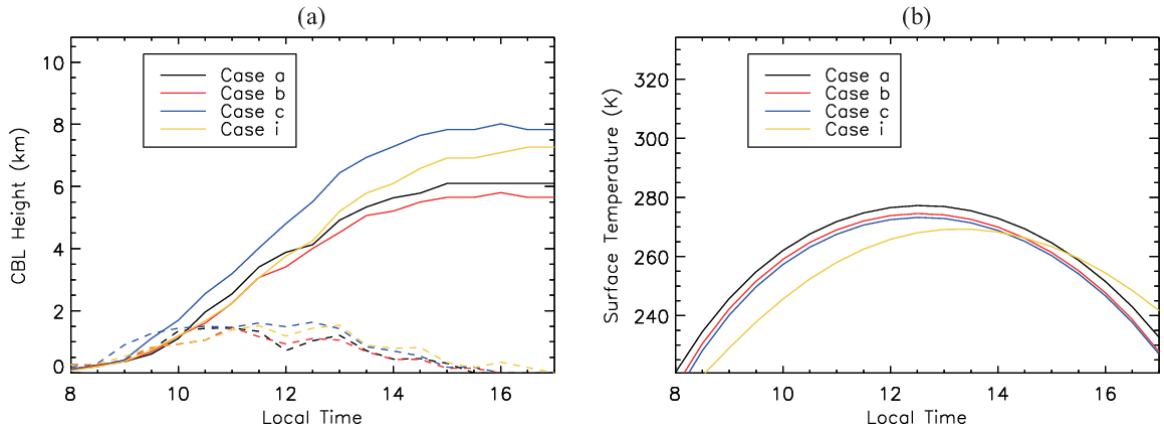

Figure 1. Evolutions of (a) CBL height (km) and (b) surface temperature (K) with time in the Martian daytime for the four Hinson cases. Dashed lines in (a) are the corresponding time derivatives of the CBL heights (km/h) with time.

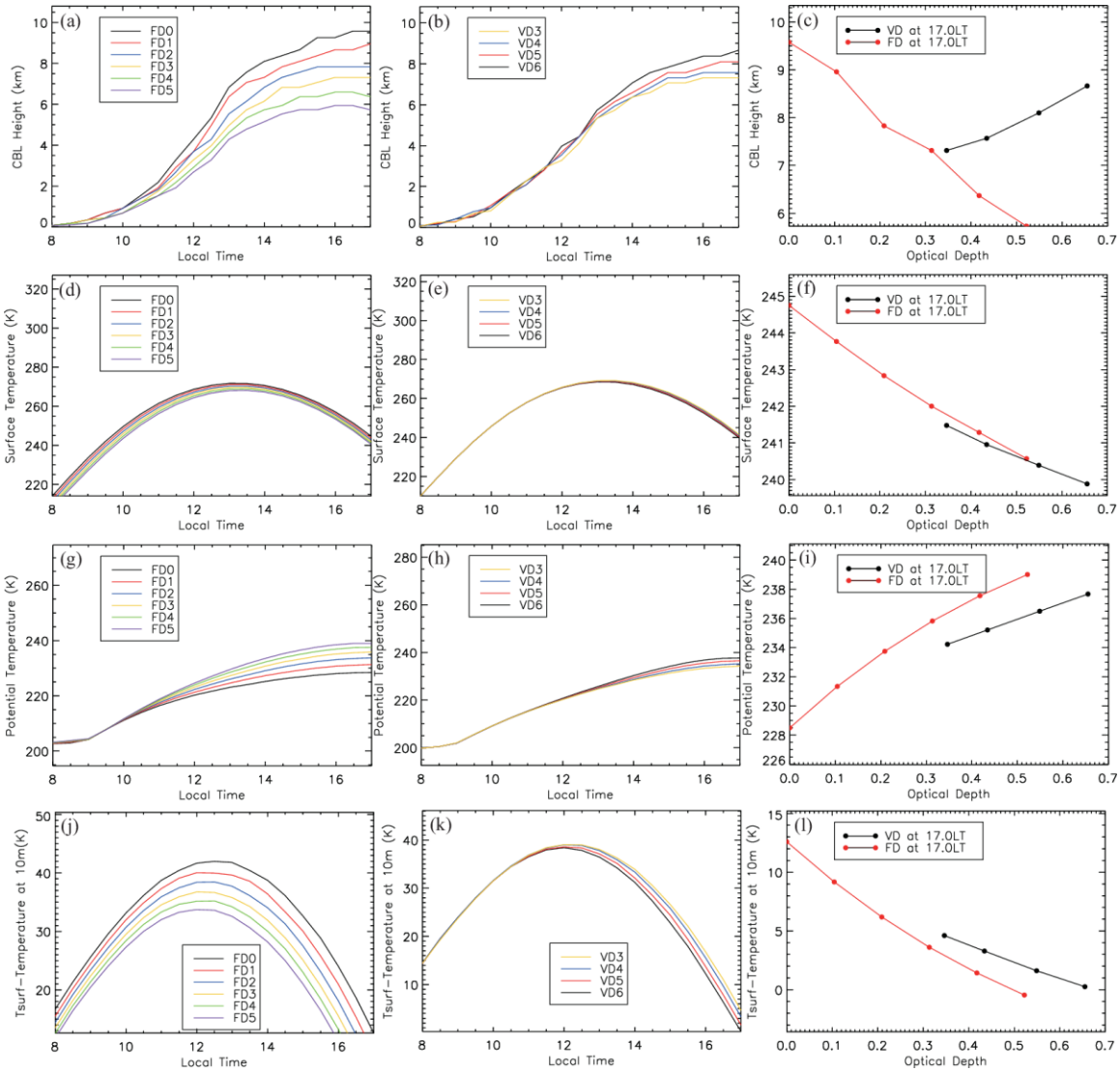

Figure 2. The evolution of (top row) the CBL height, (second row) the surface temperature, (third row) the mixed layer average potential temperature, and (bottom row) the difference between the surface temperature and the (kinetic) air temperature at 10m. All plots in the left-hand column show output as a function of local time for the Fixed Dust (FD) cases (see key for the meaning of line color), in the central column are for the Variable Dust (VD) cases as a function of local time, and in the right-hand column show both the FD and VD cases at 1700LT (labeled as 17.0LT) as a function of the instantaneous optical depth. In all cases, lateral domain averages are shown. See text for meaning of the FD and VD labels. The time varying domain mean optical depths for the VD cases is shown in Figure 4.

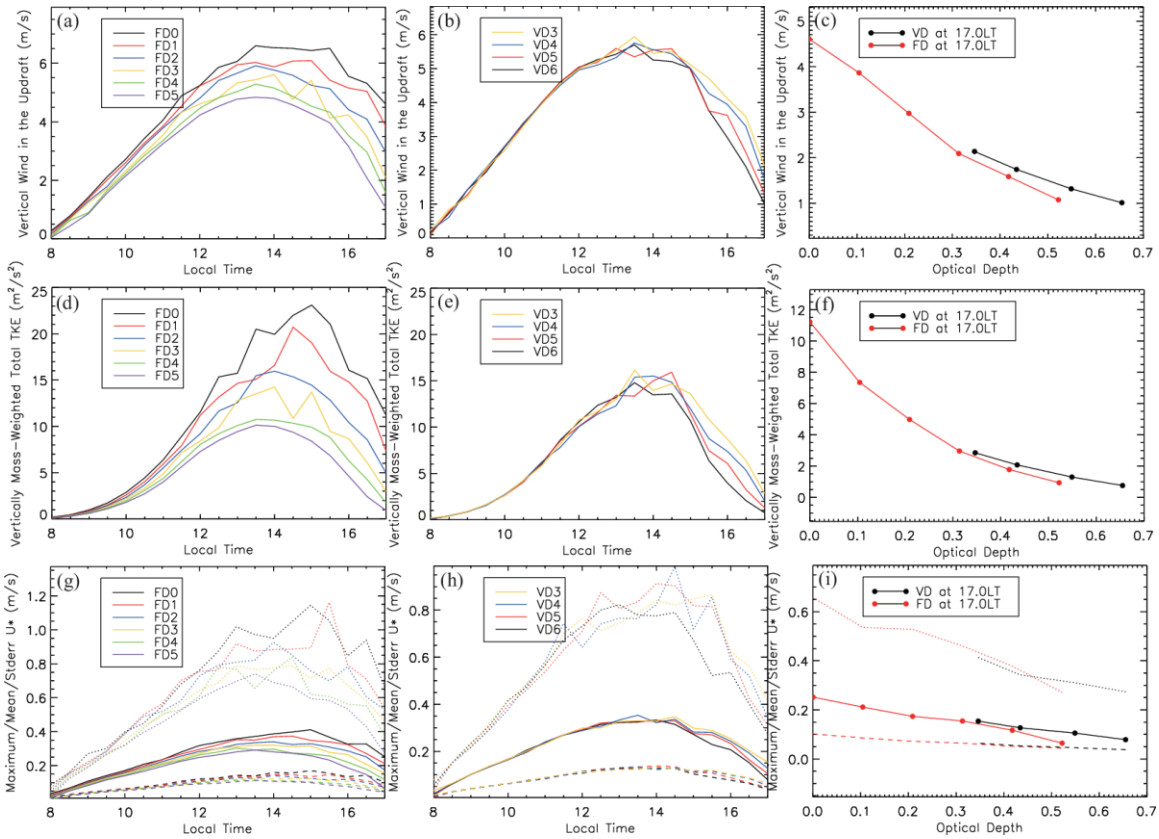

Figure 3. The evolution of (top row) updraft wind speeds, (second row) the ML average TKE, (third row) the mean (dashed line), maximum (dotted line), and standard deviation (solid line) of the surface frictional velocity (u*). The meaning of the columns and of the line colors is otherwise the same as for Figure 2.

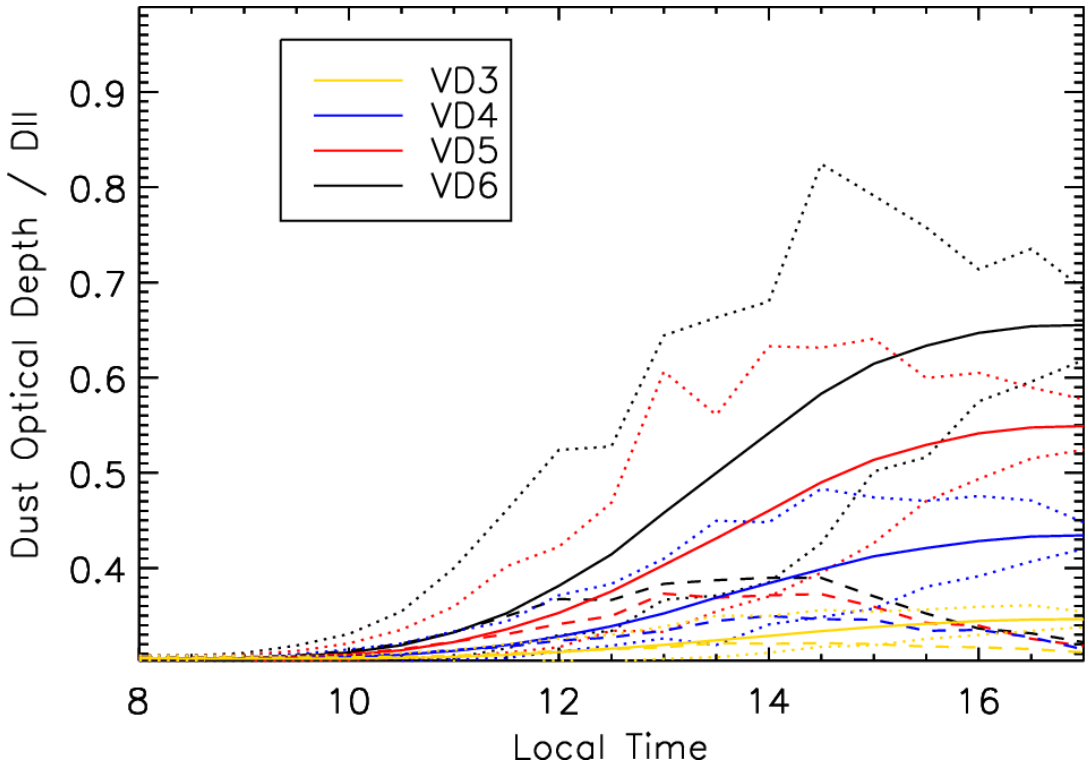

Figure 4. The variation of the mean (solid lines), minimum (lower dotted lines), and maximum (upper dotted lines) dust optical depth in the variable dust (VD) cases as a function of local time. For reference, the domain average total visible column optical depth at 1430 LT for cases VD3, VD4, VD5, and VD6 is roughly 0.3, 0.4, 0.5, and 0.6, respectively. The optical depth is not constant in time due to the interactive injection of dust into the atmosphere from the surface. The dashed lines indicate the Dust Inhomogeneity Index (DII), which we define as the standard deviation of dust optical depth for the domain divided by the averaged dust optical depth. Note that the DII value has been translated by a value of 0.3 so it can be plotted with the same y axis (*i.e.,* the DII shown = actual DII + 0.3).

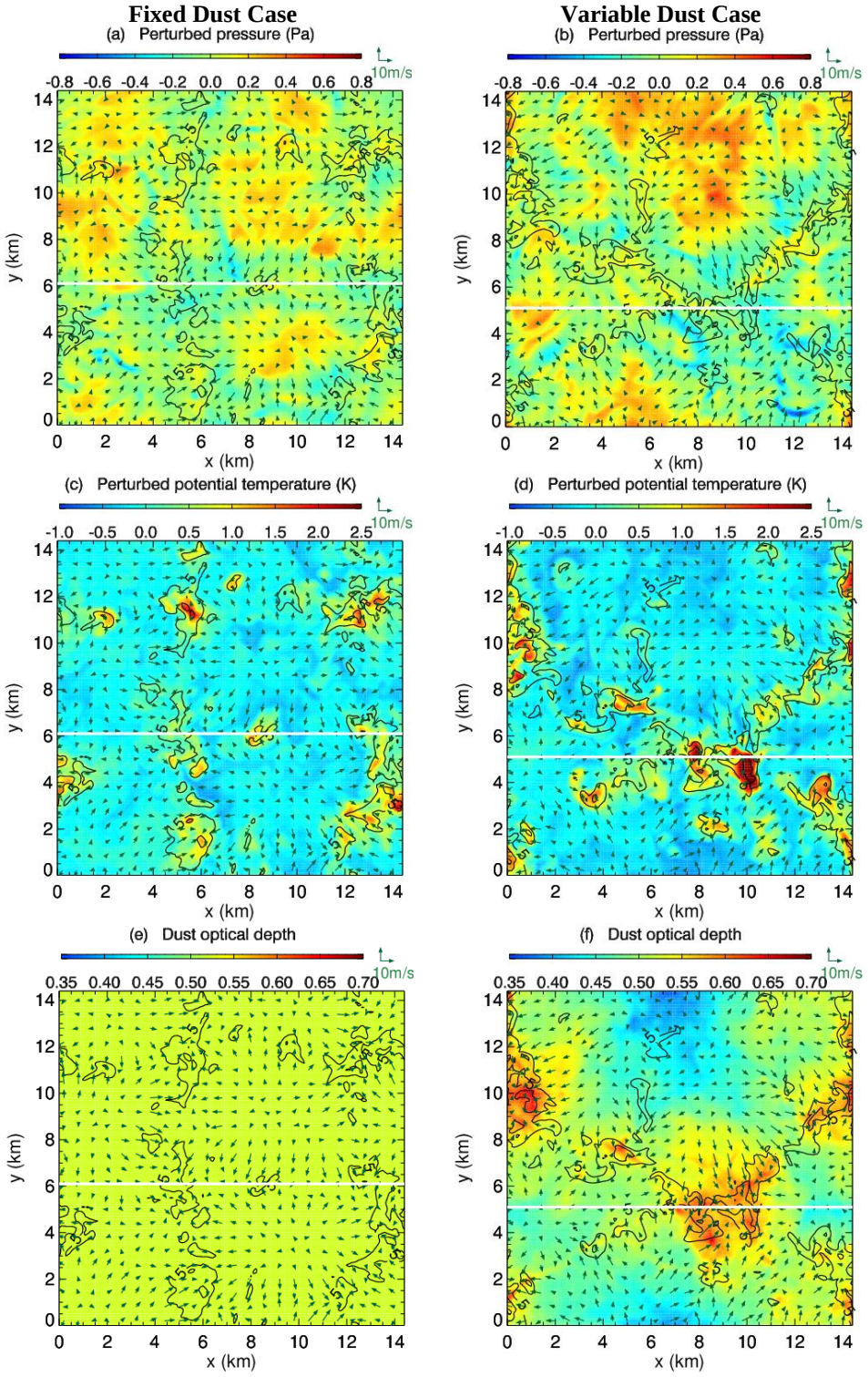

Figure 5. Comparison of LES output at 1330LT from (left column) the fixed dust "FD5" case and (right column) variable dust "VD6" case (see text for the case label definitions), both with domain average τ=0.5 optical depth. Panels (a) and (b) show the perturbation pressure at ~70 m above the surface, (c) and (d) show the perturbation potential temperature

at ~2 km above the surface, and (e) and (f) show the column-integrated dust optical depth. In all cases, the black vectors indicate the horizontal wind at ~70 m above the surface. The black contour lines show areas of strong updrafts at ~2 km above the surface, with the outer contours showing areas with >5m/s upwelling (inner contours are at >10 and >15m/s) . The horizontal white lines across each plot indicate the location of the cross sections through each LES shown in Figure 6.

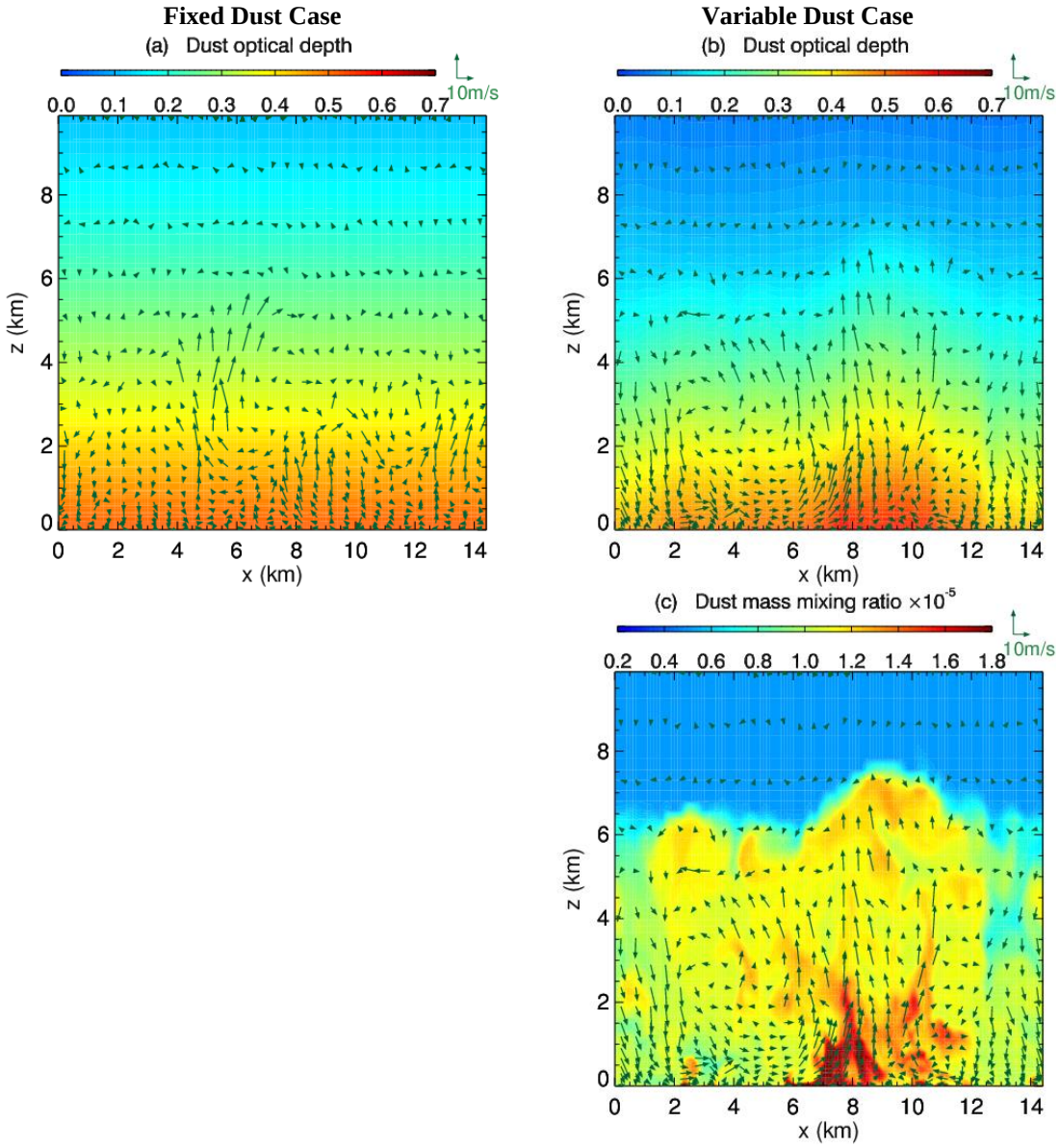

Figure 6. Cross sections of (a) and (b) the incremental dust optical depth (*i.e.*, the value in each plot indicates the total visible optical depth of dust from the top of the atmosphere down to that point in the atmosphere), and (c) the dust mass mixing ratio. Panel (a) is for the fixed dust FD5 case while panels (b) and (c) are for the variable dust VD6 case. The mass mixing ratio is not shown for the fixed dust case since it is by definition laterally uniform and nearly uniform in the vertical. The black vectors in each plot represent the horizontal and vertical (x-z) wind field. The cases shown are from the same LES at the same local time as Figure 5. The location of the cross sections are indicated in Figure 5 by the white horizontal lines.

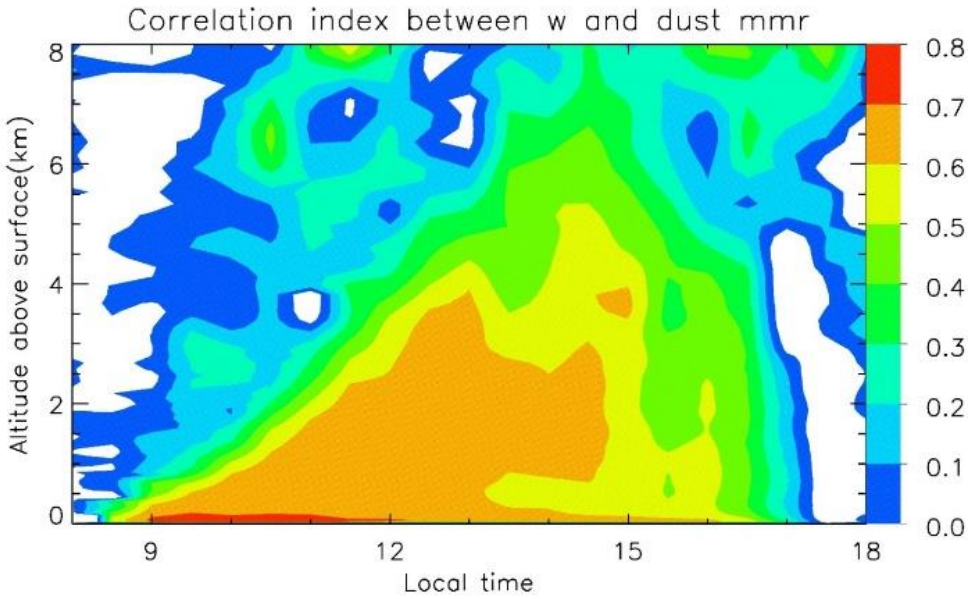

Figure 7. The correlation index between the vertical wind speed and the dust mass mixing ratio for the VD6 case as a function of local time and altitude.

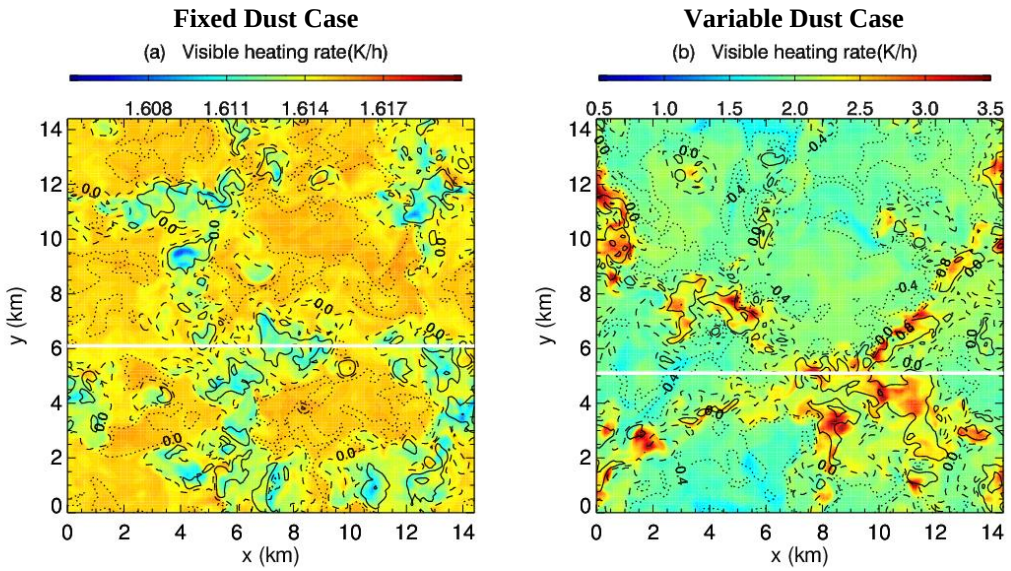

Figure 8. Visible heating rate in units of Kelvin per hour (K/h) (color shading) and perturbation potential temperature (contour) at roughly 1 km above the surface from (a) the fixed dust FD5 case and (b) the variable dust VD6 case at 1330LT. For the potential temperature, dotted, dashed and solid lines indicate negative, 0, and positive values, respectively. The white horizontal lines indicate the location of the cross sections displayed in Figure 9.

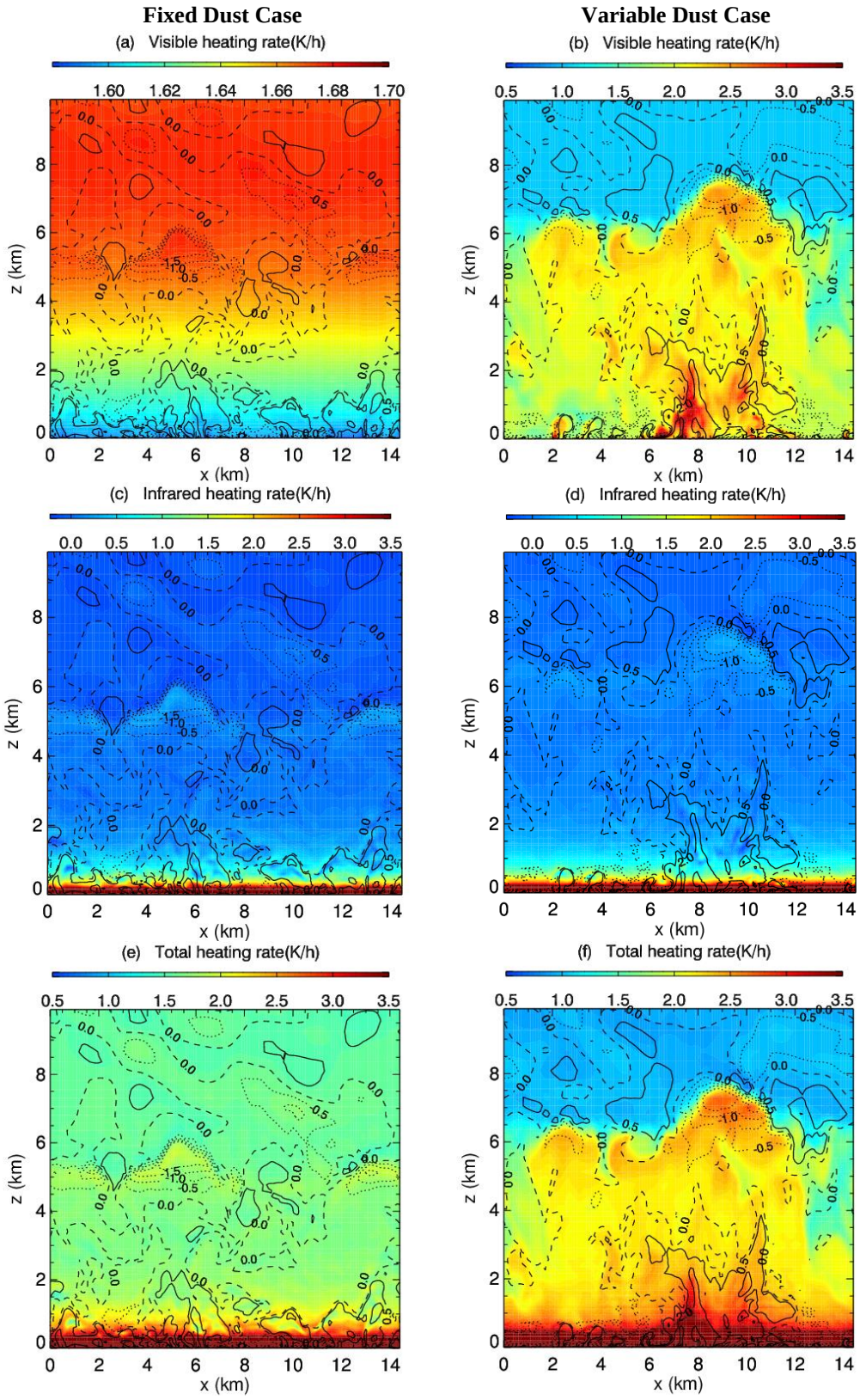
Fixed Dust Case
Variable Dust Case
(a) Visible heating rate(K/h)
(b) Visible heating rate(K/h)
(c) Infrared heating rate(K/h)
(d) Infrared heating rate(K/h)
(e) Total heating rate(K/h)
(f) Total heating rate(K/h)
z (km)
x (km)

1

Figure 9. Cross sections of the (a and b) visible, (c and d) infrared, and total (e and f) heating rates for the FD5 (left column) and VD6 (right column) cases. For all plots, the contours show the perturbation potential temperature, with dotted, dashed and solid lines indicating negative, 0, and positive values, respectively. The profiles are located within the domains shown in Figure 8 and their locations are indicated by the white horizontal lines.

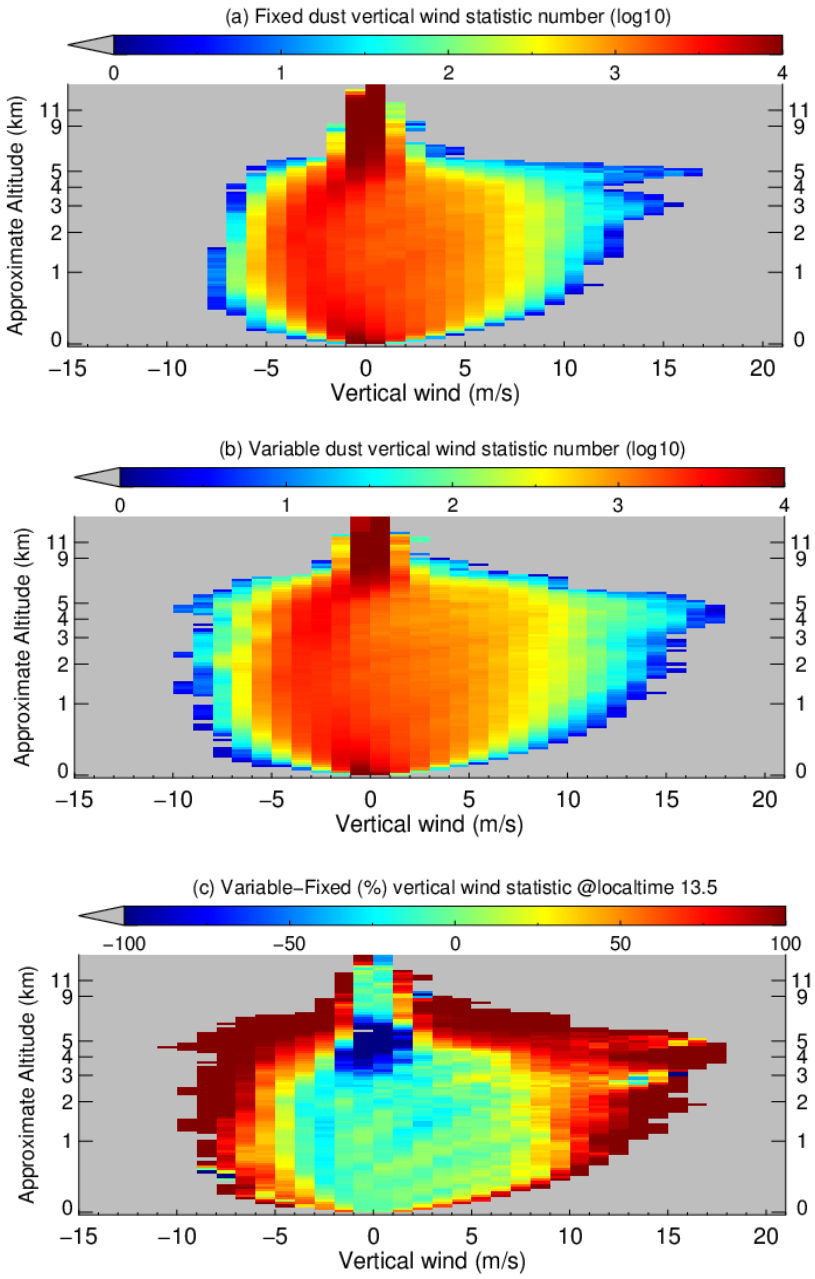

Figure 10. Variation of the vertical wind speed frequency of occurrence with altitude and vertical wind speed at local time 1330 LT, using a bin size of 1m/s. (a) fixed dust scenario with dust optical depth of 0.5, (b) variable dust scenario with averaged dust optical depth of ~0.5 and (c) the relative variable minus fixed case difference in percentage normalized by the variable dust case. The vertical wind speed frequency of occurrence is simply the number of grid cells at each level that have vertical wind within a given speed bin, plotted on a log10 scale (there are 21,025 total grid cells at each model level). The speed is binned with an increment of 1m/s.

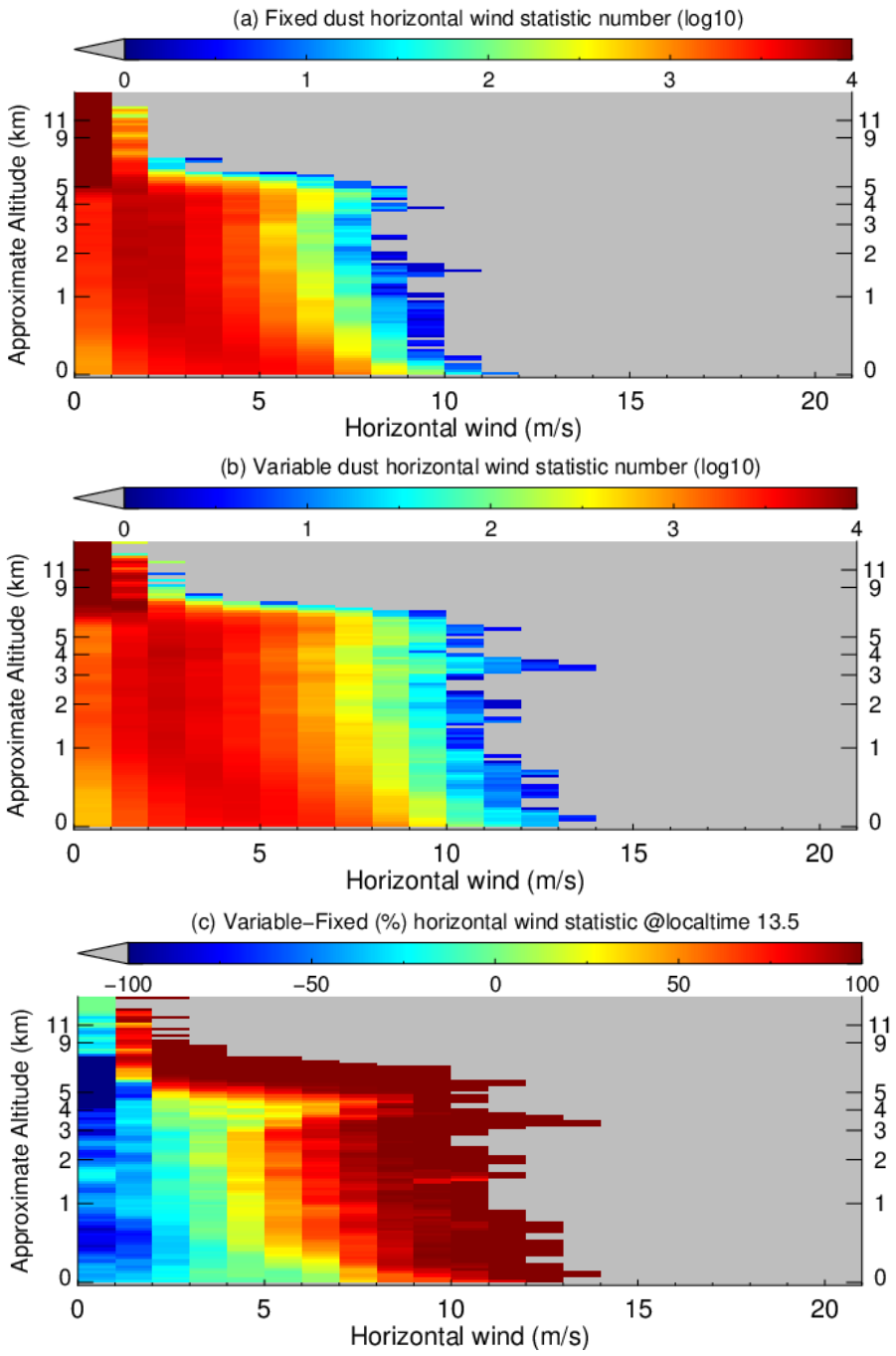

Figure 11. Same as Figure 10 but for the horizontal wind.

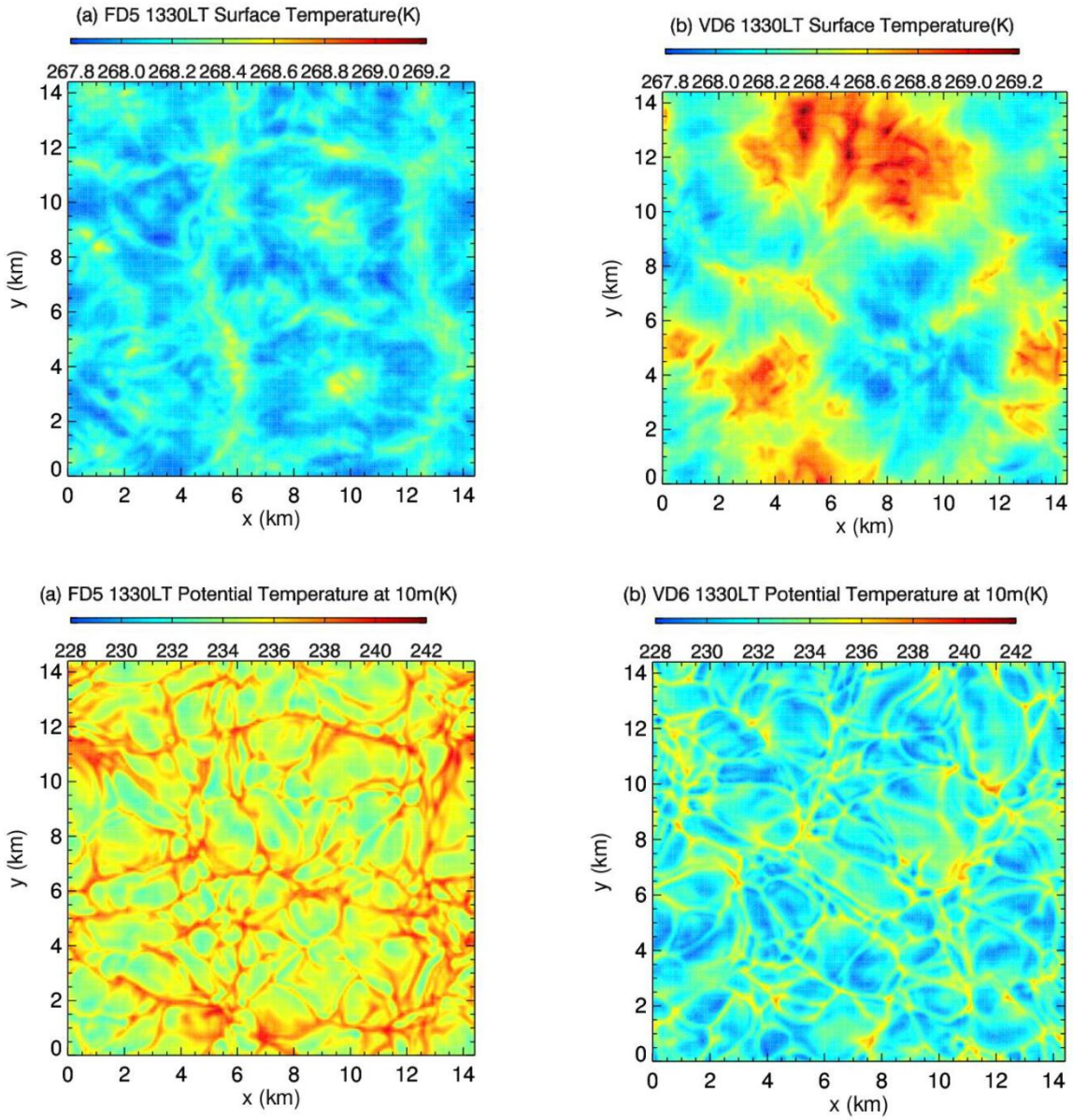

Figure 12. Surface temperatures (top row) and lowest layer air potential temperature (bottom row) at 1330LT for the FD5 (left column) and VD6 (right column) cases.

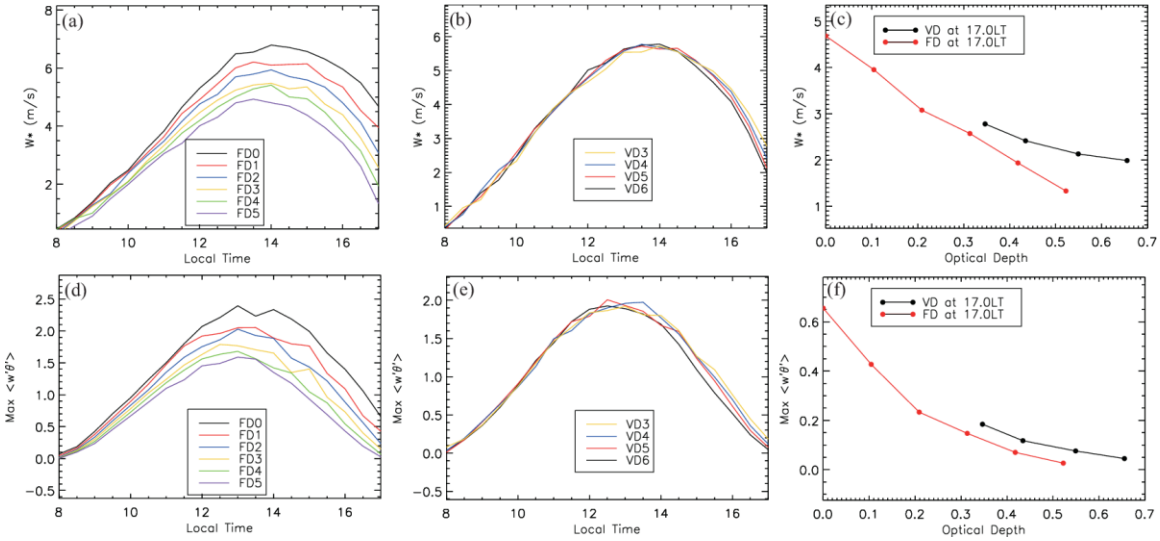

Figure 13. The evolution of (top row) the modified Deardorff velocity, W*, and (bottom row) the maximum vertical turbulent heat flux. The meaning of the columns and of the line colors is otherwise the same as for Figure 2. W* is a measure of the vertical turbulent wind scale, as defined by Eqn. 11 in Section 5.2.

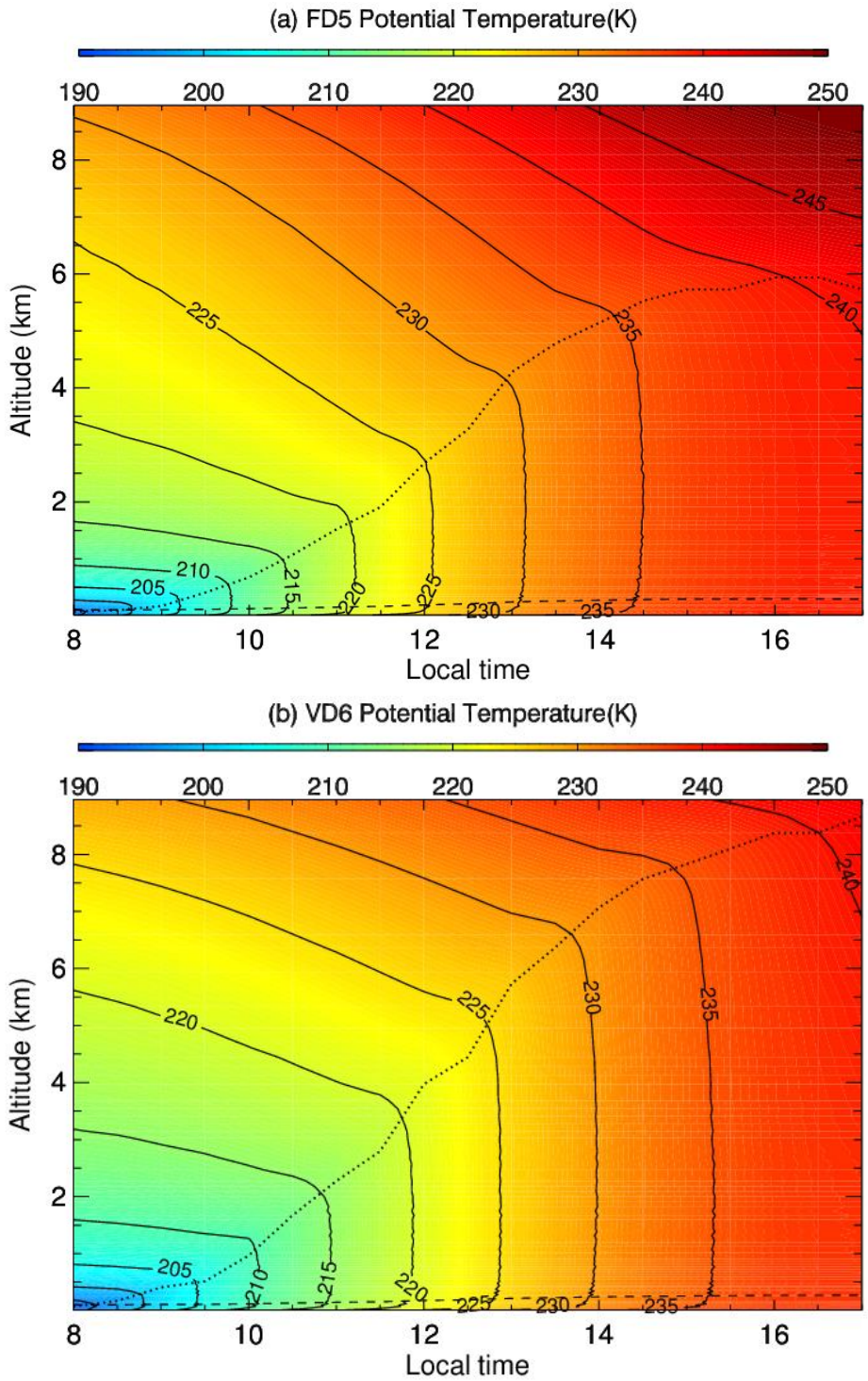

Figure 14. Domain average potential temperature as a function of altitude and local time for the (a) FD5 and (b) VD6 cases. Dashed lines and dotted lines indicate the super-adiabatic layer near the surface and the CBL top respectively.

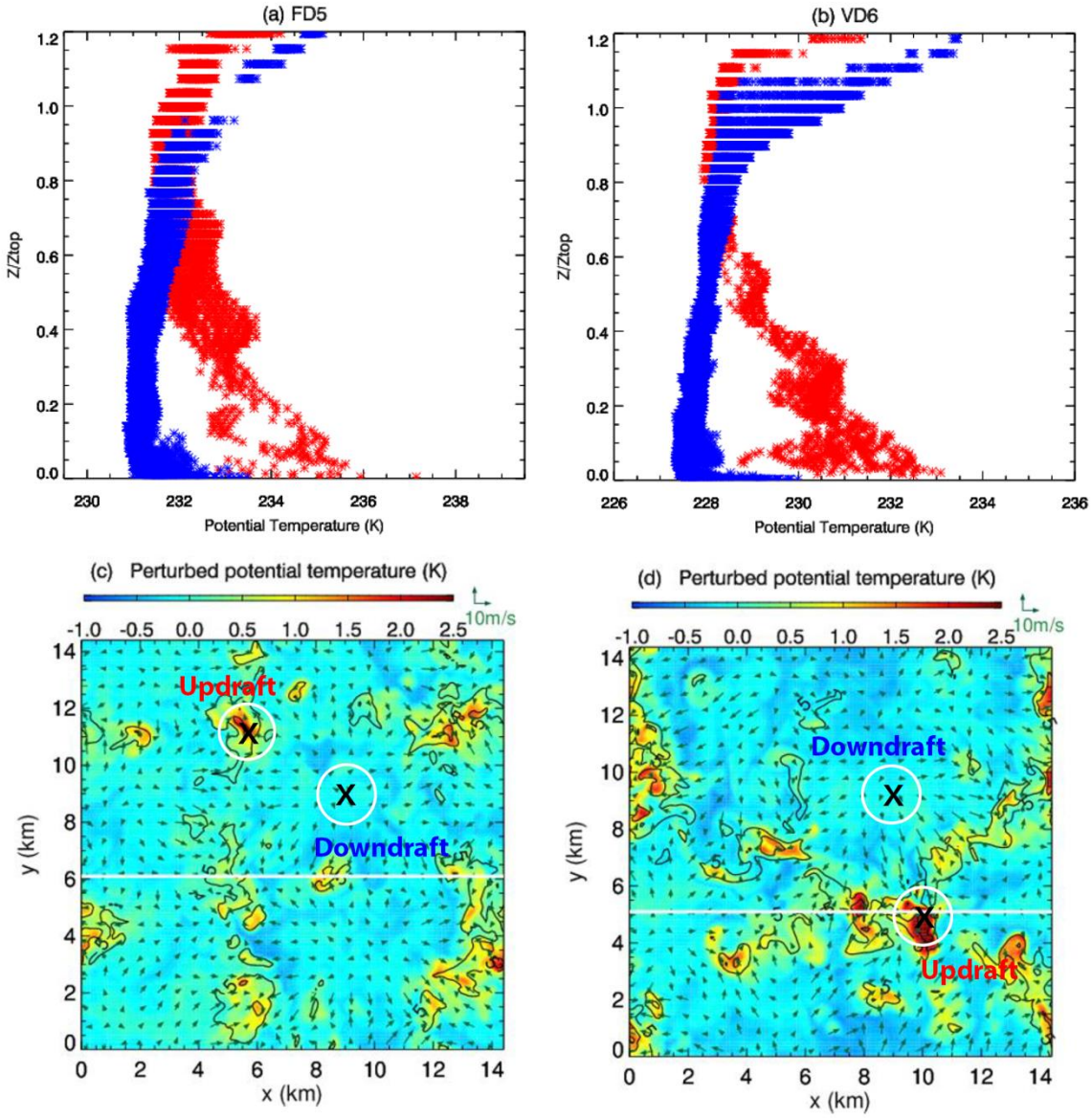

Figure 15. The potential temperature within (red) updrafts and (blue) downdrafts at 1330LT in the (a) FD5 fixed dust case and (b) the VD6 variable dust case. Updrafts are defined here as grid cells with updraft speeds exceeding 2.5× the standard deviation and downdrafts for which the downdraft speed excessed 0.5× the standard deviation. In both cases, only winds with the selected areas, indicated by white circles in panels (c) and (d), are included. The colored fields in panels (c) and (d) are the 2km potential temperature with the black arrows indicating the horizontal wind at 70m (these panels are the same as Fig. 5 c and d except for the updraft / downdraft labeling).

1

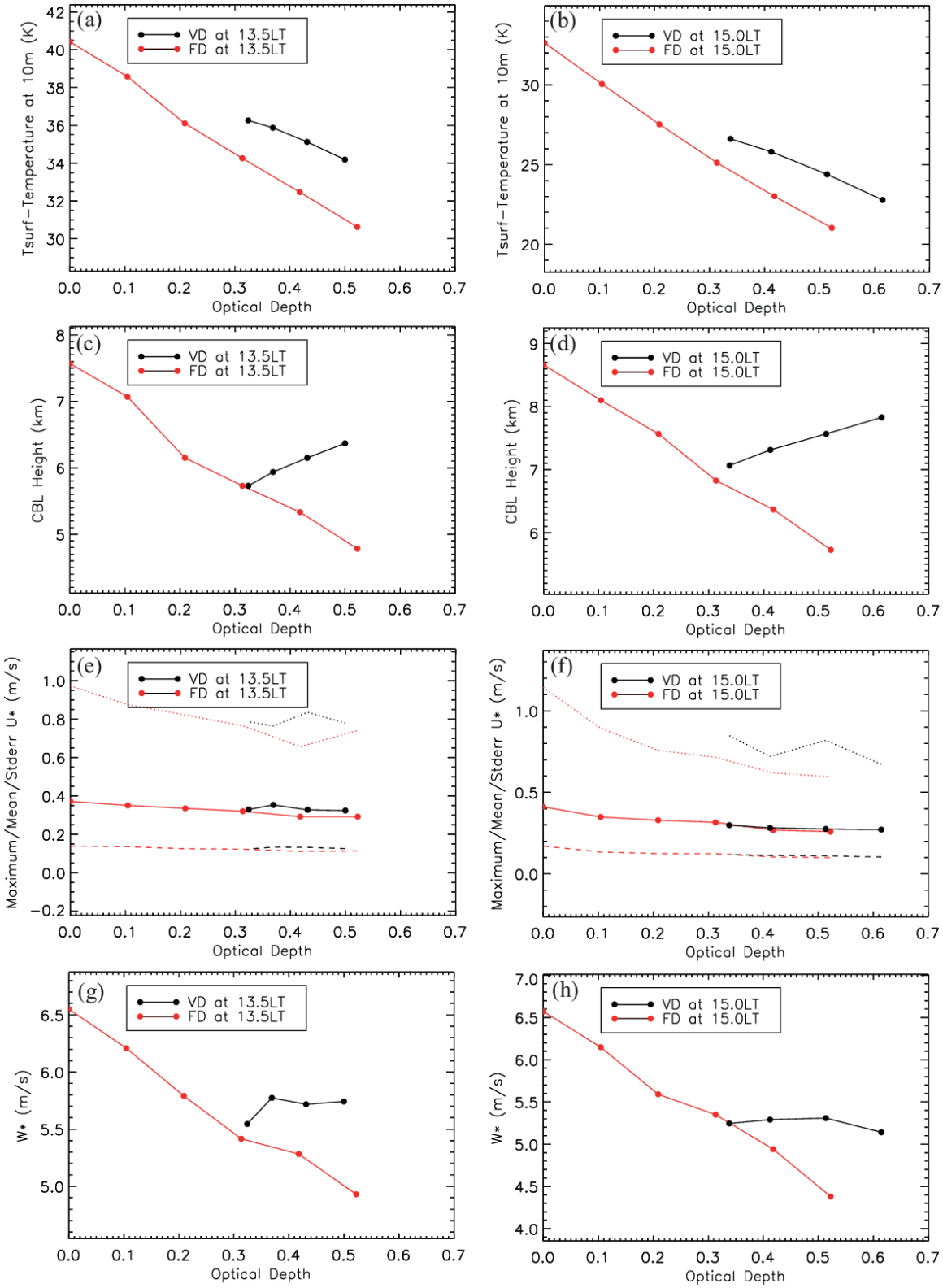

2

3 Figure 16. The dependence of various CBL parameters upon optical depth for the FD and
4 VD cases at (left column) 1330LT (labeled as 13.5LT) and (right column) 1500LT

(labeled 15.0LT). The parameters shown are (top row) the surface-atmosphere temperature contrast, (second row) the CBL height, (third row) the drag velocity, and (bottom row) the modified Deardorff velocity. Values for these parameters and with the same plot style are shown for 1700LT in Figures 2 and 3.

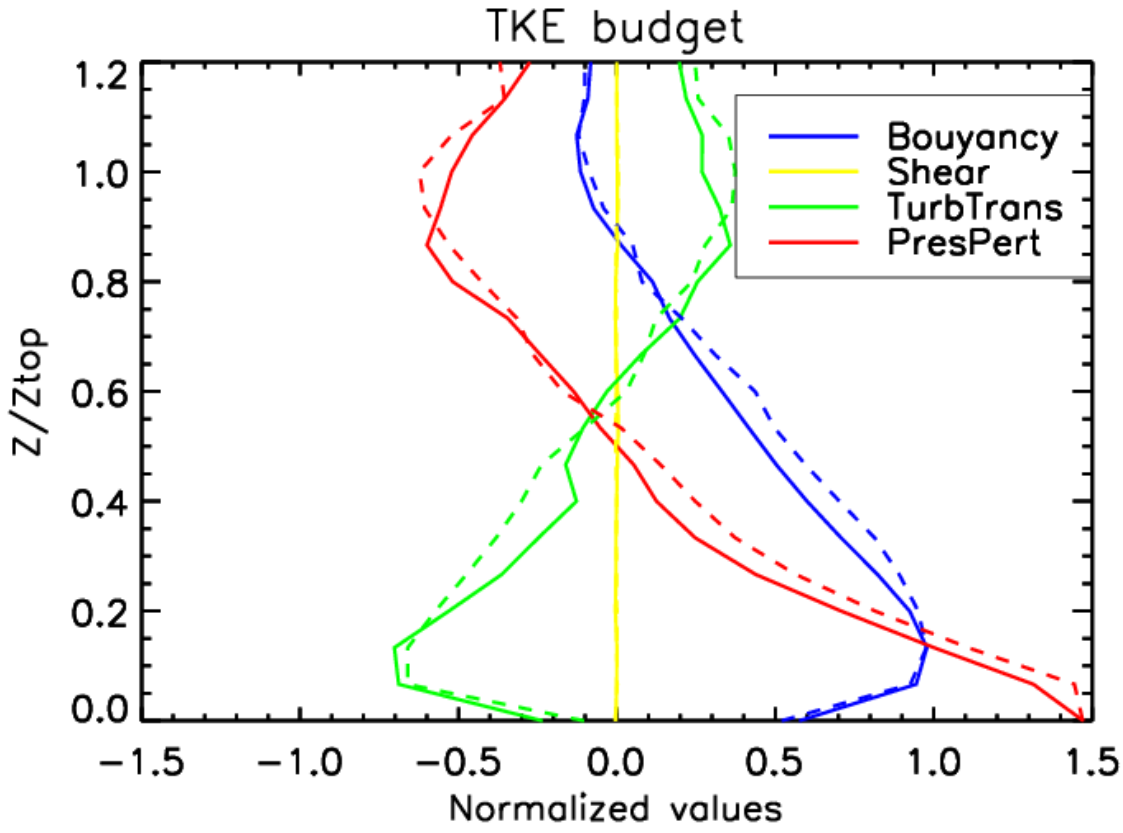

Figure 17. The four normalized TKE budget terms. Solid lines for variable dust case and dashed lines for fixed dust case. All profiles are averaged between 0900 and 1600 LT (output every 30 minutes).

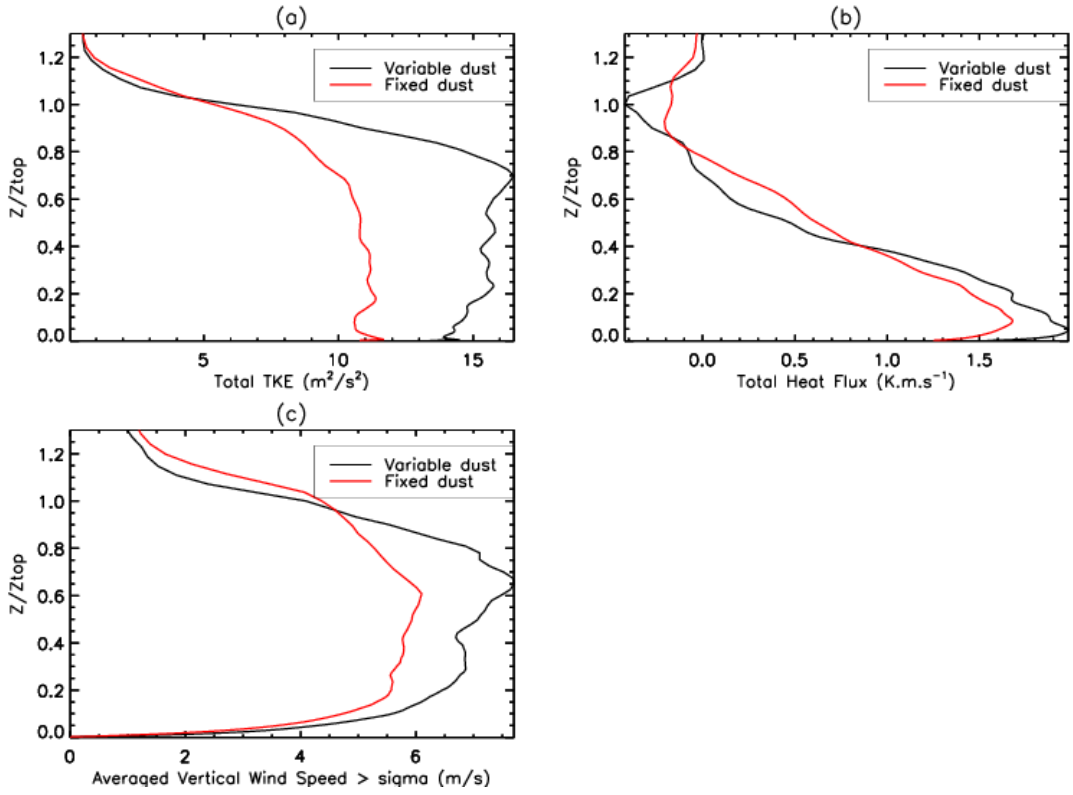

Figure 18. Variations of horizontally averaged (a) TKE (m^2/s^2), (b) total vertical eddy heat flux (Km/s), (c) averaged vertical wind speed in the updraft (m/s) with altitude at local time 1330 LT for fixed (red line) and variable (black line) dust cases. Updrafts are defined as locations where the vertical wind speed exceeds one standard deviation (or "sigma" as noted on the label to panel (c)).

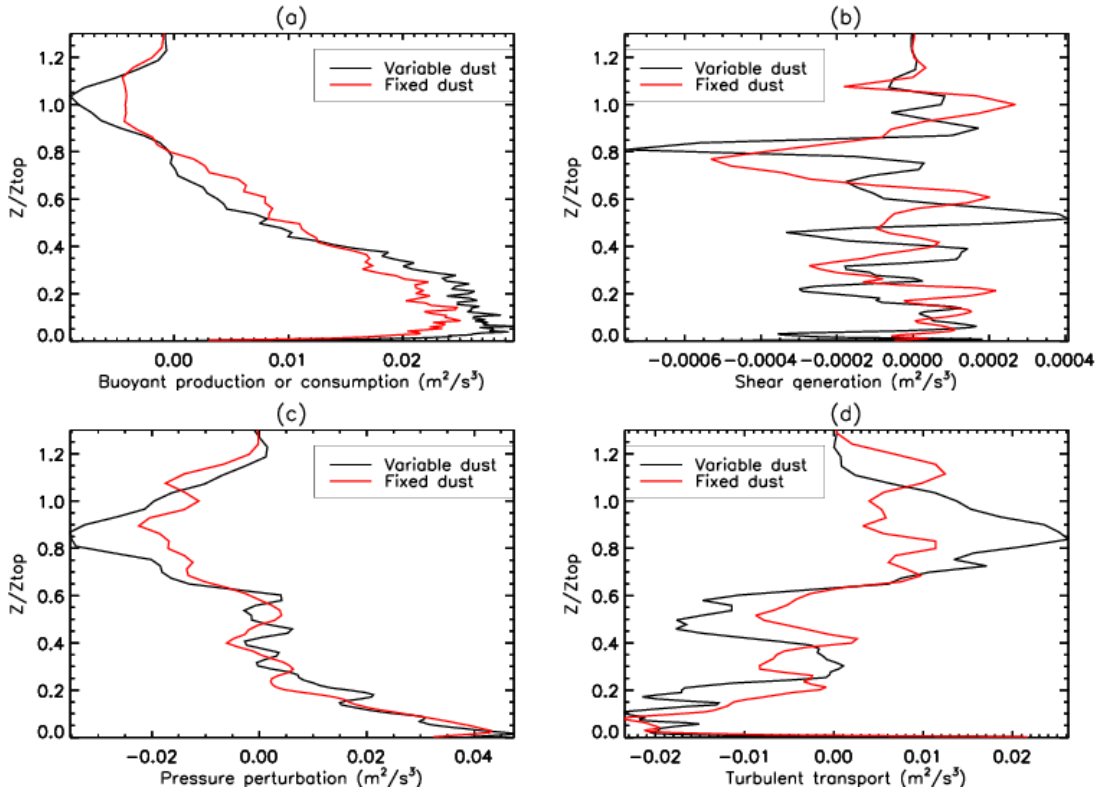

Figure 19. Same as Figure 18 but for the four TKE budget terms.

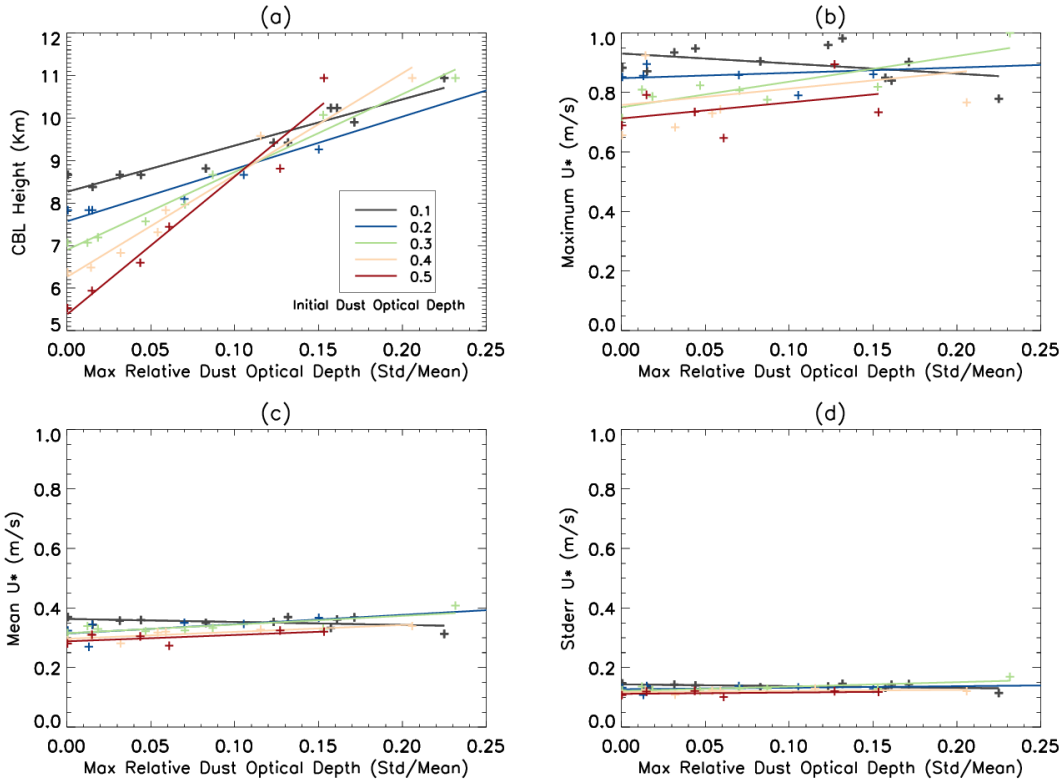

Figure 20. Variation of (a) CBL heights (km) at ~17 LT, and (b) maximum, (c) mean, (d) standard error of the friction velocity u* at 1300-1500 LT, with maximum dust inhomogeneity index values for different initial dust optical depth.

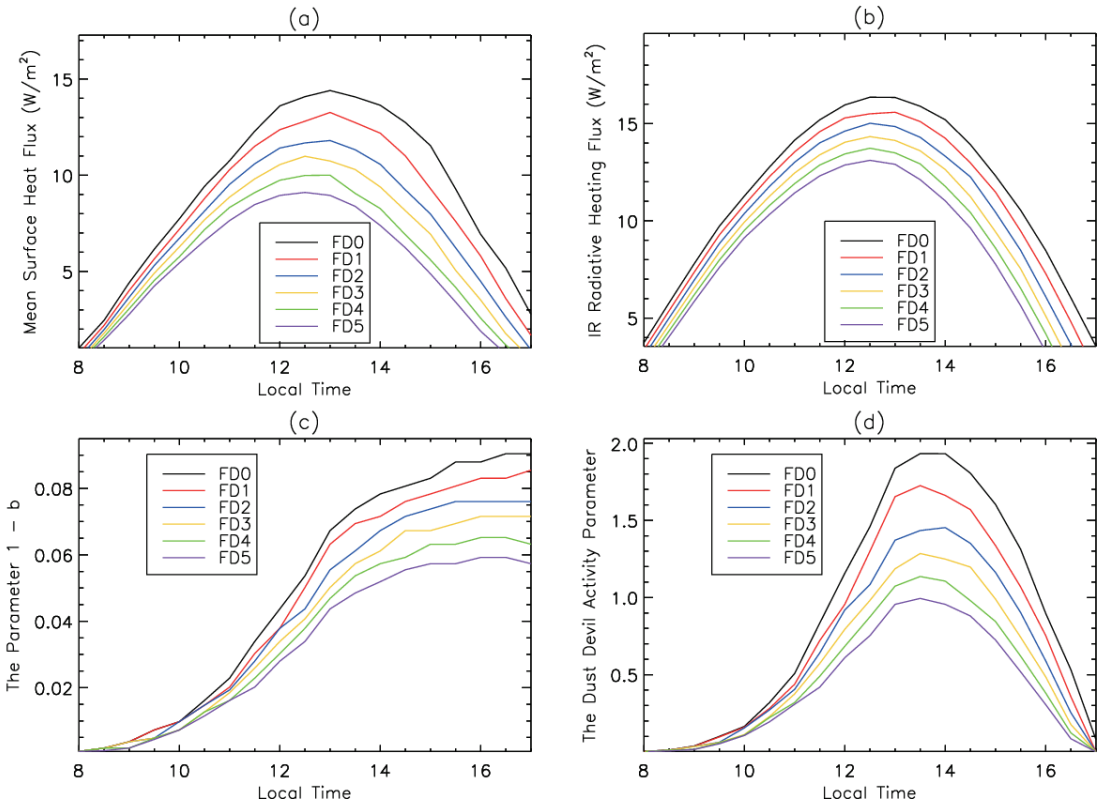

Figure 21. The evolution of (a) sensible heat flux (W/m2), (b) the infrared heating of the lowest 1km of the CBL (W/m2), (c) the thermodynamic efficiency parameter for dust devils following *Renno et al*. [1998], and (d) the dust devil activity factor generated from the product [*Newman et al*., 2002] of the thermodynamic efficiency parameter and the sum of the sensible and radiative heating of the lower CBL (the sum of the quantities in panels (a) and (b)). The cases shown are from the fixed dust (FD) ensemble.

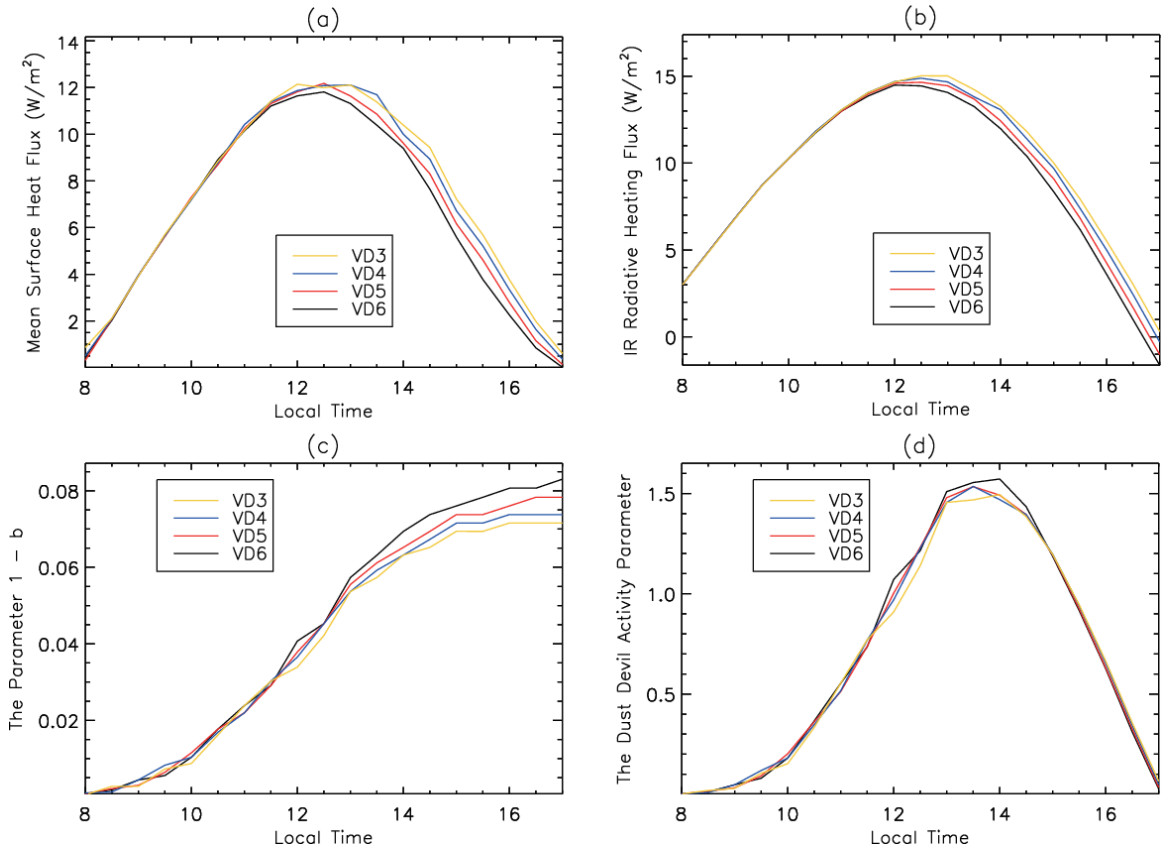

Figure 22. Same as Figure 21 but for the variable dust (VD) ensemble.

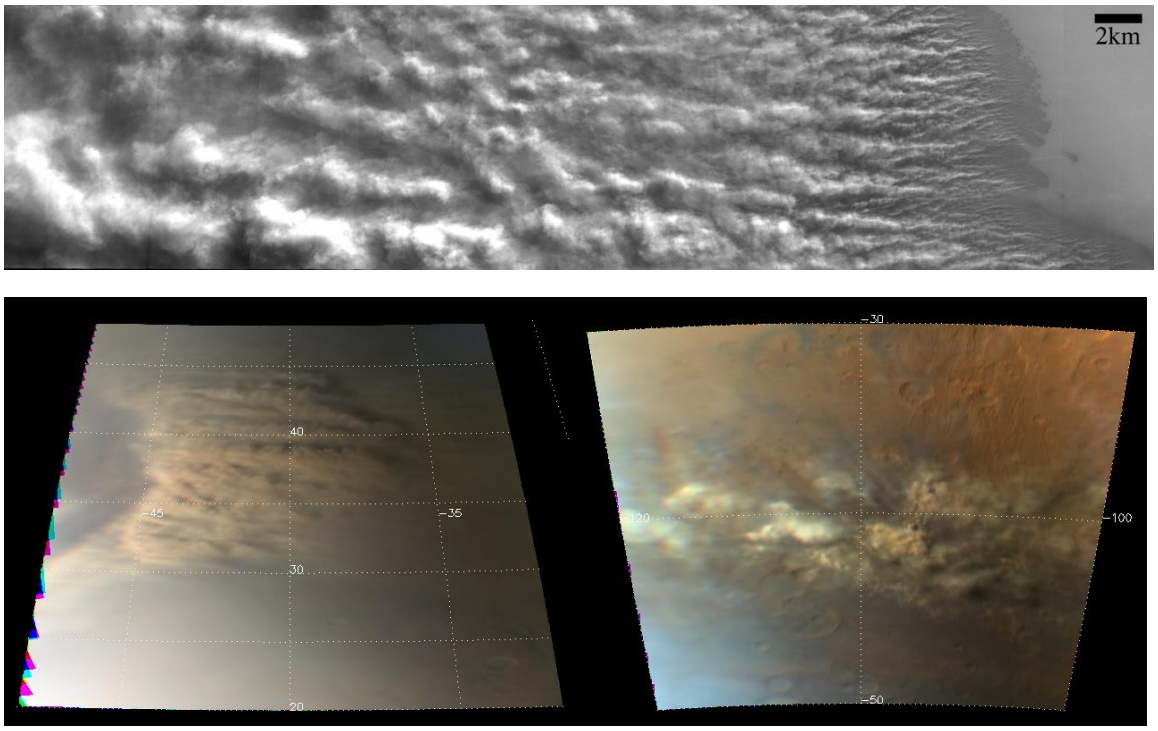

Figure 23. Images of lateral dust inhomogeneity in the Martian atmosphere on various scales. (top) THEMIS visible image of dust lifting in the high southern latitudes. Plume structures on scales from several km down to a few 100m are visible. THEMIS image number V00874006. (bottom left) Color composite image derived from MARCI image G06_020693_2052_MA_00N029W showing dust lifting on 10-100km scale at Ls=205.2 MY=30. (bottom right) Color composite created from MARCI image B16_015883_0243_MA_00N109W (Ls=24.3 MY=30).